J. Fluid Mech. (2024), *vol*. 990, A5, doi:10.1017/jfm.2024.507

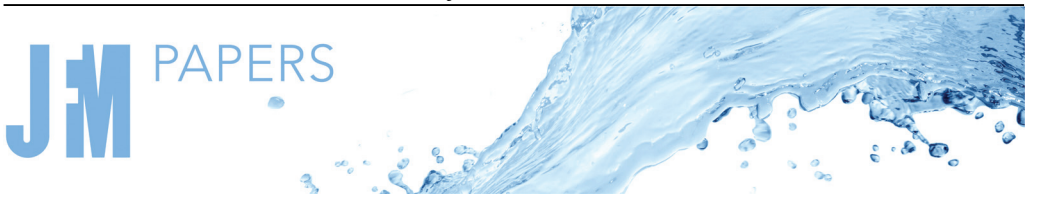

Transport of inertial spherical particles in compressible turbulent boundary layers

Ming Yu[1], **Lihao Zhao**[2], **Xianxu Yuan**[1],† **and Chunxiao Xu**[2],†

[1]State Key Laboratory of Aerodynamics, China Aerodynamics R&D Center, Mianyang 621000, PR China

[2]Key Laboratory of Applied Mechanics, Ministry of Education, Institute of Fluid Mechanics, Department of Engineering Mechanics, Tsinghua University, Beijing 100084, PR China

(Received 2 January 2024; revised 7 May 2024; accepted 19 May 2024)

In the present study, we perform direct numerical simulations of compressible turbulent boundary layers at free stream Mach numbers 2–6 laden with dilute phase of spherical particles to investigate the Mach number effects on particle transport and dynamics. Most of the phenomena observed and well-recognized for inertia particles in incompressible wall-bounded turbulent flows – such as near-wall preferential accumulation and clustering beneath low-speed streaks, flatter mean velocity profiles, and trend variation of the particle velocity fluctuations – are identified in the compressible turbulent boundary layer as well. However, we find that the compressibility effects are significant for large inertia particles. As the Mach number increases, the near-wall accumulation and the small-scale clustering are alleviated, which is probably caused by the variations of the fluid density and viscosity that are crucial to particle dynamics. This can be affected by the fact that the forces acting on the particles with viscous Stokes number greater than 500 are modulated by the comparatively high particle Mach numbers in the near-wall region. This is also the reason for the abatement of the streamwise particle velocity fluctuation intensities with the Mach numbers.

Key words: high-speed flow, compressible turbulence, particle/fluid flow

1. Introduction

Particle-laden turbulent boundary layer flows are ubiquitous in nature and wide realms of engineering applications (Rudinger 2012): to name but a few, the formation and evolution of sandstorms (Cheng, Zeng & Hu 2012; Liu & Zheng 2021), aircraft in extreme weather conditions (Cao, Wu & Xu 2014), chemical industries (Baltussen *et al.* 2018) and supersonic combustors (Feng *et al.* 2023*a*,*b*). Under the conditions of low volume fraction and low mass loadings, the dispersed particles smaller than the Kolmogorov length scales

† Email addresses for correspondence: yuanxianxu2023@163.com, xucx@tsinghua.edu.cn

can be regarded as dilute suspensions of point particles, passively transported by the turbulent flows, which is usually referred to as 'one-way coupling', and can be simulated by the point-particle approach under the Eulerian–Lagrangian framework (Elghobashi 1994; Balachandar 2009; Balachandar & Eaton 2010; Kuerten 2016). Depending on their densities and diameters, particles with different inertia respond to multi-scale turbulent motions to form various particle clusters (Crowe, Troutt & Chung 1996; Balkovsky, Falkovich & Fouxon 2001; Salazar *et al.* 2008), which in isotropic turbulence can be characterized by the Stokes number based on the Kolmogorov scale St_K, namely the ratio between the particle response time τ_p and the Kolmogorov time scale τ_K (Eaton & Fessler 1994; Goto & Vassilicos 2008; Bragg & Collins 2014).

In incompressible canonical wall turbulence, such as turbulent channels, pipes and boundary layers, the non-homogeneity and anisotropy of the turbulent fluctuations due to the restriction of the wall further complicate the motions and distributions of the particles. Early experimental and numerical investigations on one-way coupling between wall-bounded turbulence and particles have found that the departure of the particles from the fluid with their increasing inertia can be illustrated by the statistics that the particle mean streamwise velocity is higher than that of the fluid in the near-wall region, while it is lower in the outer region, leading to much flatter profiles (Rashidi, Hetsroni & Banerjee 1990; Eaton & Fessler 1994). The cross-stream particle velocity fluctuations are correspondingly weaker, indicating their incapability of following the motions of the fluid (Zhao, Marchioli & Andersson 2012). From the perspective of their accumulation, it is found that the particles incline to move towards the near-wall region and form streaky structures that resemble the low-speed streaks in the buffer region (Soldati 2005; Soldati & Marchioli 2009; Balachandar & Eaton 2010; Brandt & Coletti 2022), the degree of which is the highest for particles with $St^+ \approx 10$–80 (Soldati & Marchioli 2009), with St^+ the Stokes number under viscous scales. Marchioli & Soldati (2002) revealed that the vertical transport of the particles is highly correlated with the sweeping and ejection events in the near-wall region. The near-wall accumulation of the comparatively large particles should be attributed to the hindering of the rear ends of the quasi-streamwise vortices from the particles being transported away from the wall. Picciotto, Marchioli & Soldati (2005*b*) confirmed that the particle Stokes number determines the near-wall accumulation and clustering, and proposed that the streamwise and spanwise wall shear stress can be used to control the particle distribution. Vinkovic *et al.* (2011) showed that only when the instantaneous Reynolds shear stress exceeds a threshold, which scales approximately with the square root of the Stokes number, are the ejection events capable of bringing the particle upwards. Sardina *et al.* (2012) found that the near-wall accumulation and the clustering are closely linked with each other, and that they are, in fact, two aspects of the same process. They pointed out that the movement of particles towards the wall due to the turbophoretic drift should be balanced by their accumulating within the regions of ejection to remain in the statistical steady state, forming the directional clusters along the streamwise direction. Mortimer, Njobuenwu & Fairweather (2019) analysed the particle dynamics utilizing the probability density function, and found that particles with large Stokes numbers entering the viscous sublayer from the buffer region tend to retain their streamwise velocity and spatial organization, leading to higher streamwise velocity fluctuations of particles than those of the fluid. In the outer region, however, the correlation between the particle concentration and the flow topology is comparatively weak (Rouson & Eaton 2001).

The above-mentioned studies mainly concern particle transport by low Reynolds number channel flows. Ever-advancing computational resources enable the investigation

of transport of inertia particles at moderate to high Reynolds numbers, though still for incompressible flows. It has been revealed that the particles at different inertia respond effectively to flow structures with similar eddy turnover time, 'filtering' the smaller-scale turbulent motions. This is obvious in turbulent plane Couette flows (Bernardini, Pirozzoli & Orlandi 2013), which contain large-scale streamwise rollers even when at low Reynolds numbers. Besides the highest level of particle clustering at $St^+ \approx 25$ that responds the most efficiently to the near-wall cycles, another mode of concentration emerges in plane Couette flow with spanwise scales identical to those of the large-scale rollers. Bernardini (2014) investigated the particle distribution with different inertia at friction Reynolds number up to 1000. Although the wall-normal concentration and hence the turbophoretic drift are independent of the Reynolds number, the deposition rates are higher with increasing Reynolds number at the same Stokes number. Jie *et al.* (2022) and Motoori, Wong & Goto (2022) further confirmed that particles with different inertia respond the most significantly to the flow structures with similar turnover time in wall turbulence. Therefore, the multi-scale clustering of the particles can be characterized by the structure-based Stokes number. Berk & Coletti (2020) detected in high Reynolds number turbulent boundary layers that the particles tend to accumulate inside the upward moving ejection events for particles with a wide range of Stokes numbers, suggesting that the clustering is probably a multi-scale phenomenon. In the core region of the channel, Jie, Andersson & Zhao (2021) demonstrated that the inertial particles accumulate more preferably within the high-speed regions in the quiescent core (Kwon *et al.* 2014), but avoid the vortical structures due to the centrifugal mechanism, whose boundaries function as barriers, hindering the transport of particles.

Compressible turbulent boundary layers laden with dilute phase of particles can be encountered in such engineering applications as high-speed vehicles travelling through the rain, ice crystals and other types of particles suspending in the atmosphere, the ablation of fuselage materials generating small particles transported downstream by the high shear rate, and so on. However, related studies are comparatively scanty. In compressible isotropic turbulence, the particles are found to concentrate within the regions of low vorticity and high density, which, due to the increasing compressibility effects, are weakened by the stronger shocklets (Yang *et al.* 2014; Zhang *et al.* 2016; Dai *et al.* 2017). The shocklets are also found to modify the probability density function of the particle accelerations and lead to differences of statistics between the traces and bubbles (Wang, Wan & Biferale 2022). Similar phenomena are observed in compressible mixing layers (Dai *et al.* 2018, 2019), but due to the existence of the mean shear, the particles also cluster within the low- or high-speed streaks, depending on their appearance on either the high- or low-speed side. Xiao *et al.* (2020) investigated the particle behaviour in a spatially developed turbulent boundary layer at Mach number 2, where the near-wall accumulation and the clustering of the particles with the velocity streaks are also observed. By analysing the equation of the dilatation of particles, they found that the small particles accumulate within the low-density regions, but the large particles accumulate within the low-density regions close to the wall and high-density regions in the wake region, which is attributed to the different centrifugal effects and the variation of the fluid density. Buchta, Shallcross & Capecelatro (2019) revealed that the particle–turbulence interactions alter the local pressure intensities, which are stronger with the mass loading near the subsonic region, but weaker near the supersonic regions. The former was attributed to the increasing time-rate-of-change of fluid dilatation and the latter to the weaker turbulent kinetic energy. Li *et al.* (2023) further studied the particle-laden compressible turbulent channel flows incorporating the effects of gravity. It is found that the mean and fluctuating

particle velocities in the streamwise direction are increased, but those in the cross-stream directions are decreased due to the compressibility effects. Moreover, the particles are more likely to be clustered within the ejections and sweeping events compared with those in incompressible flows. Capecelatro & Wagner (2024) reviewed the development of the force models of single and multiple particles in compressible flows, and the flow modulations due to the presence of solid particles. This review concerned mostly the dilute suspensions of finite-sized particles using particle-resolved direct numerical simulations (DNS), especially the shock–particle interactions.

Although much has been learned about the effects of particle inertia and Reynolds numbers in incompressible wall turbulence, and those of compressibility on the particle concentration in compressible isotropic turbulence, there lacks a systematic study of the particle transport in compressible turbulent boundary layers at various Mach numbers. This serves as the motivation of the present study. In this work, we perform DNS of compressible turbulent boundary layers laden with inertial particles at free stream Mach numbers ranging from 2 to 6 to explore the effects of the Mach number on the behaviour of particles, encompassing the near-wall accumulation, clustering with the velocity streaks, statistics and dynamics. The conclusions will benefit the modelling of particle motions in engineering applications of compressible turbulence.

The remainder of this paper is organized as follows. The physical model and numerical methods utilized to perform the DNS are introduced in § 2. The features of the particle distribution, including the instantaneous distribution, near-wall accumulation and clustering behaviour, are discussed in § 3. The mean and fluctuating velocity and acceleration are presented in § 4. Finally, the conclusions are summarized in § 5.

2. Physical model and numerical methods

In the present study, we perform DNS of the compressible turbulent boundary layers with particles utilizing the Eulerian–Lagrangian point-particle method. The physical model and numerical methods for the fluid and particles will be introduced in the following subsections.

2.1. *Simulation of supersonic turbulent boundary layers*

We first introduce the governing equations and the numerical settings for the fluid phase. The compressible turbulent boundary layer flows are governed by the three-dimensional Navier–Stokes equations for Newtonian perfect gases, cast as

$$\frac{\partial \rho}{\partial t} + \frac{\partial (\rho u_i)}{\partial x_i} = 0, \tag{2.1}$$

$$\frac{\partial (\rho u_i)}{\partial t} + \frac{\partial (\rho u_i u_j)}{\partial x_j} = -\frac{\partial p}{\partial x_i} + \frac{\partial \tau_{ij}}{\partial x_j}, \tag{2.2}$$

$$\frac{\partial (\rho E)}{\partial t} + \frac{\partial (\rho E u_j)}{\partial x_j} = -\frac{\partial (p u_j)}{\partial x_j} + \frac{\partial (\tau_{ij} u_i)}{\partial x_j} - \frac{\partial q_j}{\partial x_j}, \tag{2.3}$$

where u_i is the velocity component of the fluid in the x_i direction, with $i = 1, 2, 3$ (also x, y and z) denoting the streamwise, wall-normal and spanwise directions. Here, ρ is density,

p is pressure, and E is total energy, related by the following state equations of perfect gases:

$$p = \rho RT, \quad E = C_v T + \tfrac{1}{2} u_i u_i, \tag{2.4a,b}$$

where T is temperature, R is the gas constant, and C_v is the constant volume specific heat. The viscous stresses and the molecular heat conductivity are determined by the following constitutive equations for Newtonian fluids and Fourier's law, respectively:

$$\tau_{ij} = \mu \left(\frac{\partial u_i}{\partial x_j} + \frac{\partial u_j}{\partial x_i} \right) - \frac{2}{3} \mu \frac{\partial u_k}{\partial x_k} \delta_{ij}, \quad q_j = -\kappa \frac{\partial T}{\partial x_j}, \tag{2.5a,b}$$

where μ is the viscosity, calculated by Sutherland's law, and κ is the molecular heat conductivity, determined as $\kappa = C_p \mu / Pr$.

The DNS are performed utilizing the open-source code STREAmS developed by Bernardini *et al.* (2021), using the finite difference method to solve the governing equations. The convective terms are approximated by the sixth-order kinetic energy preserving scheme (Kennedy & Gruber 2008; Pirozzoli 2010) in the smooth region and the fifth-order weighted essentially non-oscillation (WENO) scheme (Shu & Osher 1988) when the flow discontinuity is detected by the Ducros sensor (Ducros *et al.* 1999). The viscous terms are approximated by the sixth-order central scheme. The low-storage third-order Runge–Kutta scheme is adopted for time advancement (Wray 1990).

The boundary conditions are given as follows. The turbulent inlet is composed of the mean flow obtained by empirical formulas (Musker 1979) and the synthetic turbulent fluctuations using the digital filtering method (Klein, Sadiki & Janicka 2003). The no-reflecting conditions are enforced at the upper and outlet boundaries. Periodic conditions are adopted in the spanwise direction. The no-slip condition for velocity and the isothermal condition for temperature are given at the lower wall.

Herein, the free stream flow parameters are denoted by the subscript ∞. The free stream Mach number is defined as the ratio between the free stream velocity and the sound speed $M_\infty = U_\infty / \sqrt{\gamma R T_\infty}$, and the free stream Reynolds number is defined as $Re_\infty = \rho_\infty U_\infty \delta_0 / \mu_\infty$, with δ_0 the nominal boundary layer thickness at the turbulent inlet. The ensemble average of a generic flow quantity φ is marked as $\bar{\varphi}$, the corresponding fluctuations as φ', the density-weighted average (Favre average) as $\tilde{\varphi}$, and the corresponding fluctuations as φ''. The viscous scales are defined based on the mean shear stress τ_w, viscosity μ_w, and density ρ_w at the wall, resulting in the friction velocity $u_\tau = \sqrt{\tau_w / \rho_w}$, viscous length scale $\delta_\nu = \mu_w / (\rho_w u_\tau)$ and friction Reynolds number $Re_\tau = \rho_w u_\tau \delta / \mu_w$ (with δ the nominal boundary layer thickness at a given streamwise station). The flow quantities normalized by these viscous scales are denoted by the superscript $+$. Local viscous scales are defined accordingly by substituting the wall density ρ_w and wall viscosity μ_w with their local mean values, and the flow quantities normalized by these local viscous scales are marked by the superscript $*$.

The streamwise, wall-normal and spanwise sizes of the computational domain are set as $L_1 = 80\delta_0$, $L_2 = 9\delta_0$ and $L_3 = 8\delta_0$, discretized by 2400, 280 and 280 grids, respectively. The grids are distributed uniformly in the streamwise and spanwise directions, and stretched by a hyperbolic sine function in the wall-normal direction, with 240 grids clustered below $y = 2.5\delta_0$. At the inlet, the friction Reynolds number is set as $Re_{\tau 0} = 200$, according to which the free stream Reynolds number Re_∞ is calculated. The streamwise and spanwise grid intervals defined based on the viscous scales at the turbulent inlet are $\Delta x^+ = 6.67$ and $\Delta z^+ = 5.71$. The first grid off the wall is located at $\Delta y_w^+ = 0.5$,

Flow case	M_∞	T_w/T_∞	Re_δ	$Re_{\delta*}$	Re_θ	Re_τ
M2	2.0	1.712	13 098–24 879	4460–8162	1543–2947	285–504
M4	4.0	3.848	56 805–87 778	28 655–43 108	5795–8977	322–499
M6	6.0	7.408	153 112–240 250	94 000–128 679	12 800–18 712	316–462

Table 1. Flow parameters. Here, Re_δ, Re^*_δ and Re_θ are the Reynolds numbers defined by the nominal (δ), displacement (δ^*) and momentum (θ) boundary layer thicknesses.

and the grid interval in the free stream is $\Delta y^+ = 7.06$. Such grid intervals are sufficient with the presently used low-dissipative numerical schemes (Pirozzoli 2011).

The free stream Mach numbers of the turbulent boundary layers are set as $M_\infty = 2$, 4 and 6. The wall temperatures T_w are set to be constant values equal to the recovery temperature $T_r = T_\infty(1 + (\gamma - 1)rM^2_\infty)/2$, the mean wall temperature with adiabatic conditions at the given Mach number, with $\gamma = 1.4$ the specific heat ratio, $r = Pr^{1/2}$ the recovery factor, and $Pr = 0.71$ the Prandtl number. The streamwise variation of the nominal (Re_δ), displacement ($Re_{\delta*}$), momentum (Re_θ) and friction (Re_τ) Reynolds numbers in the statistically equilibrium regions are listed in table 1. Although the ranges of Re_δ, $Re_{\delta*}$ and Re_θ are different at various Mach numbers, the friction Reynolds numbers Re_τ are of the same level, which is the most important parameter in wall-bounded turbulence. Hereinafter, the results reported are obtained within the streamwise range $(60–70)\delta_0$ and the time span $240\delta_0/U_\infty$ to obtain converged statistics. The data are not collected until the simulations have been run for $1000\delta_0/U_\infty$, during which the turbulent flows are fully developed and the distributions of particles in the wall-normal direction reach steady states, as we will demonstrate subsequently.

In figure 1(*a*) we present the van Driest transformed mean velocity obtained by the integration

$$u^+_{1,VD} = \frac{1}{u_\tau}\int_0^{\tilde{u}_1}\left(\frac{\bar{\rho}}{\bar{\rho}_w}\right)^{1/2}\mathrm{d}u_1, \tag{2.6}$$

along with values reported by Bernardini & Pirozzoli (2011) at $M_\infty = 2$ and $Re_\tau \approx 450$ for comparison. For all the cases considered, the van Driest transformed mean velocity profiles are well collapsed and consistent with the reference data below $y^+ = 100$, obeying the linear law in the viscous sublayer, and the logarithmic law in the log region (if any). The disparity in the wake region can be ascribed to the slightly lower friction Reynolds number Re_τ in the present study. The mean temperatures $\bar{T}$ are shown in figure 1(*b*), manifesting zero gradients close to the wall due to the quasi-adiabatic thermal condition and monotonic decrement as it approaches the outer edge of the boundary layer. The mean temperature profiles are well collapsed with the generalized Reynolds analogy proposed by Zhang *et al.* (2014) that relates the mean temperature and the mean velocity:

$$\frac{\bar{T}}{T_\infty} = \frac{T_w}{T_\infty} + \frac{T_{rg} - T_w}{T_\infty}\frac{\bar{u}}{U_\infty} + \frac{T_\infty - T_{rg}}{T_\infty}\left(\frac{\bar{u}}{U_\infty}\right)^2, \tag{2.7}$$

where T_{rg} is the generalized total temperature

$$T_{rg} = T_\infty + r_g\frac{U^2_\infty}{2C_p}, \tag{2.8}$$

with r_g the generalized recovery coefficient.

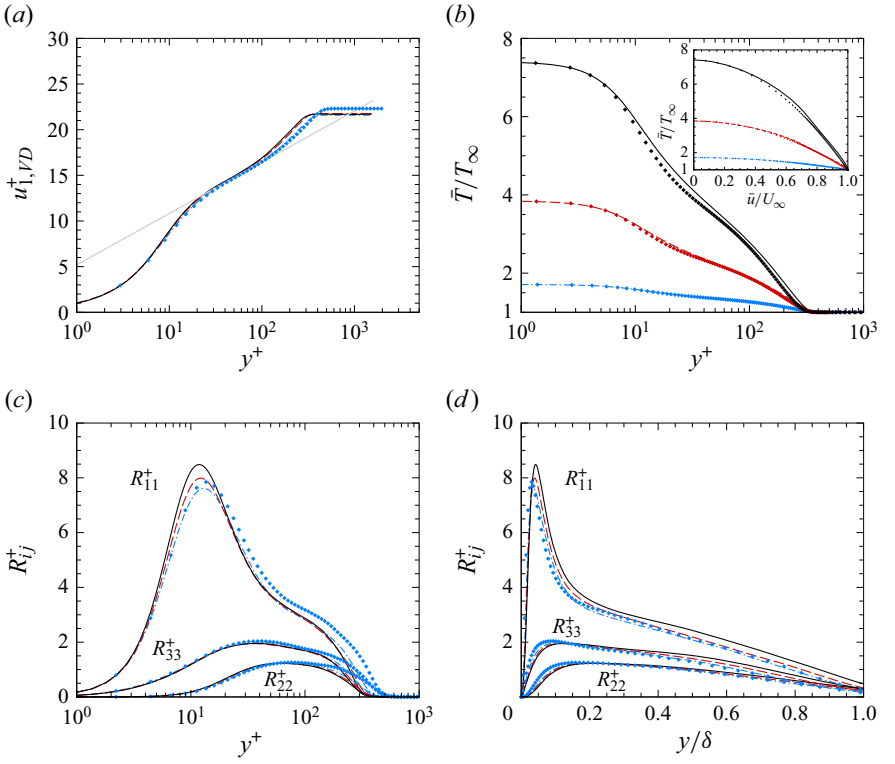

Figure 1. Wall-normal distributions of (*a*) van Driest transformed mean velocity $u^+_{1,VD}$, (*b*) mean temperature $\bar{T}/T_\infty$, (*c*,*d*) Reynolds stresses R^+_{ij}. Blue dash-dotted lines indicate case M2; red dashed lines indicate case M4; black solid lines indicate case M6. Grey lines in (*a*) indicate logarithmic law $2.44\ln(y^+) + 5.2$. Symbols in (*a*,*c*,*d*) indicate reference data from Bernardini & Pirozzoli (2011) at $M_\infty = 2$ and $Re_\tau \approx 450$; symbols in (*b*) indicate mean temperature obtained by the generalized Reynolds analogy.

Figures 1(*c*) and 1(*d*) display the distributions of the Reynolds stresses $R^+_{ij} = \overline{\rho u''_i u''_j}/\tau_w$ for the three cases, amongst which those of case M2 show agreement with the reference data reported by Bernardini & Pirozzoli (2011) in the near-wall region when plotted against the viscous coordinate (figure 1*c*), and also in the outer region when plotted against the global coordinate (figure 1*d*), except for the slightly lower peaks of R^+_{11} due to the lower Reynolds number. The Reynolds stresses are weakly dependent on the Mach number, showing a slight increment of the inner peaks with the Mach number. This is consistent with the previous studies of Cogo *et al.* (2022) and Yu, Xu & Pirozzoli (2019).

2.2. *Particle simulations in the Lagrangian framework*

The dispersed phase considered herein is composed of heavy spherical particles with infinitesimal volume and mass fractions, thereby disregarding the inter-particle collisions and the feedback effects from the particles to the fluid (Kuerten 2016). In the one-way coupling approximation, the trajectories and the motions of the spherical particles are solved by the equations

$$\frac{\mathrm{d}r_{p,i}}{\mathrm{d}t} = v_i, \quad \frac{\mathrm{d}v_i}{\mathrm{d}t} = a_i, \tag{2.9a,b}$$

with $r_{p,i}$, v_i and a_i denoting the particle position, velocity and acceleration. We consider merely the Stokes drag force induced by the slip velocity, while neglecting the other components such as the lift force, Basset history force and virtual mass force due to the large density of particles compared with that of the fluid (Maxey & Riley 1983; Armenio & Fiorotto 2001; Mortimer *et al.* 2019), cast as

$$a_i = \frac{f_D}{\tau_p}(u_i - v_i), \tag{2.10}$$

where $\tau_p = \rho_p d_p^2/18\mu$ is the particle relaxation time, d_p is the particle diameter, and ρ_p is the particle density. The coefficient f_D is estimated as

$$f_D = (1 + 0.15\,Re_p^{0.687})H_M, \tag{2.11}$$

$$H_M = \begin{cases} 0.0239M_p^3 + 0.212M_p^2 - 0.074M_p + 1, & M_p \le 1, \\ 0.93 + \dfrac{1}{3.5 + M_p^5}, & M_p > 1 \end{cases} \tag{2.12}$$

incorporating the compressibility effects, as suggested by Loth *et al.* (2021), with $Re_p = \rho\,|u_i - v_i|\,d_p/\mu$ and $M_p = |u_i - v_i|/\sqrt{\gamma RT}$ being the particle Reynolds and Mach numbers, respectively. Note that we have neglected the rarefied effects, for according to a preliminary estimation and the DNS results, particle Knudsen numbers rarely reach higher than 0.01, the criterion where the rarefied effects should be taken into account. The high Reynolds number modification incorporating the effects of the fully turbulent wake (Clift & Gauvin 1971) has also been disregarded, for the particle Reynolds numbers are always lower than 100.

We adopt the same strategy in the time advancement of the particle equations as the fluid phase using the third-order low-storage Runge–Kutta scheme. Trilinear interpolation is used to obtain information about the fluid at the particle position (Eaton 2009; Bernardini 2014). We performed DNS of particles in turbulent channel flows for validation; for details, refer to Appendix A. The initial positions of the particles in the simulation are distributed randomly within $y = 2\delta_0$, with their initial velocities set to be the same as those of the fluid. The perfectly elastic collisions are assumed when the particles hit the wall. Periodic conditions are imposed as in the fluid phase in the spanwise direction. When the particles pass through the upper boundary and the flow outlet, they are recycled to the flow inlet with a random wall-normal and spanwise position below $y = \delta_0$, and the same velocity as that of the fluid at that location so as to retain the total number of particles. As mentioned in the previous subsection, the flow statistics reported hereinafter are obtained within the range $(60\text{–}70)\delta_0$, where the particle fields are considered to be fully developed, with the validation presented in Appendix B.

The dispersed phase contains seven particle populations with the same particle numbers $N_p = 10^6$. As reported in table 2, these particle populations share the identical diameter $d_p = 0.001\delta_0$ and various density ratios ρ_p/ρ_∞ ranging from 20 to 50 000. Within the nominal boundary layer thickness, the volume fraction of the dispersed particle phase is approximately 4×10^{-7}, and the mass fraction ranges from 8×10^{-6} to 0.02, suggesting the appropriateness of the one-way coupling approximation. In figure 2(*a*), we present the ratios between the particle diameter and the Kolmogorov scale d_p/η, which are lower than 1.0 across the boundary layer, satisfying the requirements of the point-particle approach (Maxey & Riley 1983; Kuerten 2016). When normalized by the local viscous length scale, as shown in figure 2(*b*), the particle diameters d_p^* are approximately 0.185 at the wall and

Type	d_p/δ_0	ρ_p/ρ_∞	St_∞			St^+			$St_{K,w}$		
			M2	M4	M6	M2	M4	M6	M2	M4	M6
P1	0.001	20	0.011	0.041	0.11	0.065	0.14	0.27	0.031	0.068	0.12
P2	0.001	100	0.056	0.20	0.55	0.33	0.70	1.33	0.15	0.34	0.63
P3	0.001	500	0.28	1.01	2.74	1.63	3.52	6.63	0.77	1.70	3.17
P4	0.001	2500	1.40	5.07	13.70	8.15	17.60	33.15	3.86	8.50	15.85
P5	0.001	10000	5.60	20.28	54.78	32.59	70.44	132.59	15.46	34.00	63.41
P6	0.001	20 000	11.21	40.56	109.56	65.18	140.81	265.19	30.91	67.99	126.83
P7	0.001	50 000	28.02	101.39	273.90	162.94	352.21	662.97	77.28	169.98	317.07

Table 2. Particle diameters, density ratios and Stokes numbers.

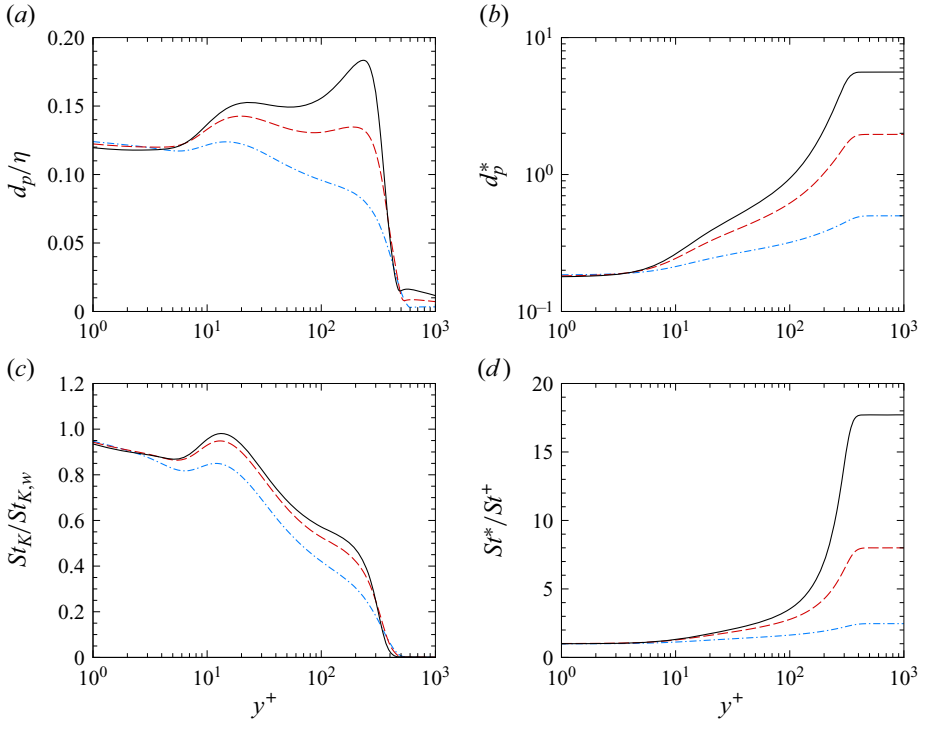

Figure 2. Wall-normal distribution of the particle diameters (*a*) d_p/η and (*b*) d_p^*, and the relative particle Stokes numbers (*c*) St_K/St_{Kw} and (*d*) St^*/St^+. Blue dash-dotted lines indicate case M2; red dashed lines indicate case M4; black solid lines indicate case M6.

increase monotonically towards the edge of the boundary layer, with the highest value 4.734 at $M_\infty = 6$.

The different particle densities lead to the disparity in the particle relaxation time τ_p. In table 2, we list three sets of particle Stokes numbers,

$$St_\infty = \tau_p/\tau_\infty, \quad St^+ = \tau_p/\tau_\nu, \quad St_{K,w} = \tau_p/\tau_{K,w}, \tag{2.13a–c}$$

representing the ratio between the particle relaxation time τ_p and the characteristic time scale of the flow under the outer scale $\tau_\infty = \delta_0/U_\infty$, under the viscous scale $\tau_\nu = \delta_\nu/u_\tau$, and under the Kolmogorov scale at the wall $\tau_{K,w} = (\mu_w/\varepsilon_w)^{1/2}$. Amongst these

parameters, $St_{K,w}$ is a crucial parameter in isotropic turbulence, determining the features of the particle dynamics and accumulation (Balachandar & Eaton 2010; Brandt & Coletti 2022), whereas St^+ is commonly used in wall turbulence. For particles in incompressible wall turbulence without viscosity stratification, both τ_p and τ_ν are constant. However, this is not the case for the presently considered flow, for the viscosity μ is a function of temperature, complicating the evaluation of the particle inertia. In figures 2(*c*,*d*), we present the distributions of St_K and St^+ compared with their values at the wall. Due to the lower dissipation, St_K decreases monotonically away from the wall, showing weak Mach number dependence. The St^* values, on the other hand, increase with the wall-normal coordinate, and escalate with the Mach number, indicating that the response of the particle to the turbulent fluctuation of the fluid flow is varying across the boundary layer due to the stratification of the mean density and viscosity, especially near the edge of the boundary layer.

3. Instantaneous and statistical particle distributions

3.1. *Instantaneous particle distribution*

We first present in figure 3 the instantaneous distribution of the particle populations P1, P4, P5 and P6, and the fluid density ρ in case M4, along with the edge of the boundary layer marked by $u_1 = 0.99U_\infty$. For population P1, with the lowest particle density ρ_p and Stokes number St^+, the particles appear to be uniformly distributed within the region where the fluid density is lower than that of the free stream value, even inside the small 'blobs' that are spatially separated from the turbulent boundary layer, but fail to fill in the regions between these 'blobs' and the primary turbulent regions of the boundary layers, the region where the density is the free stream value but the momentum is lower. As the Stokes number increases to $St^+ \approx 17.6$ (P4) and 70.44 (P5), the particles accumulate close to the wall, thereby leading to their lower concentration at higher locations. Due to their comparatively larger inertia away from the wall (recall figure 2*d*), some of the particles with high vertical velocities are capable of escaping from the low-fluid-density regions and reaching the free stream. This is especially the case for population P6 ($St^+ \approx 140.81$) with an even larger particle density, a considerable portion of which can be ejected to the free stream, while the tendency of wall accumulation is weakened. The variation of the particle distributions with the Stokes numbers in other flow cases is similar to this case, showing non-monotonic behaviour of near-wall accumulation. This is consistent with previous studies in incompressible wall turbulence (Marchioli & Soldati 2002; Bernardini 2014).

We would like to remark on the resemblance in the instantaneous distributions of the low Stokes number particles and the fluid density. It has been shown that in the limit of small volumetric loading, the concentration field c (number of particles per volume) of the particles can be approximated as (Ferry & Balachandar 2001, 2002)

$$\frac{\partial c}{\partial t} + \frac{\partial c v_j}{\partial x_j} = c\,\frac{\partial u_i}{\partial x_i}. \tag{3.1}$$

Under the conditions $\rho_p/\rho_f \gg 1$ and $St^+ \ll 1$, the velocities of the fluid and particles are approximately the same, $v_i \approx u_i$, with the deviation being of the order of $O(\tau_p)$ in outer scales. For the presently considered compressible flow over a quasi-adiabatic flat plate, the flow dilatation can be disregarded in comparison with the vortical and shear (Yu *et al.* 2019; Yu & Xu 2021), so the right-hand side of (3.1) can be neglected, leading to the

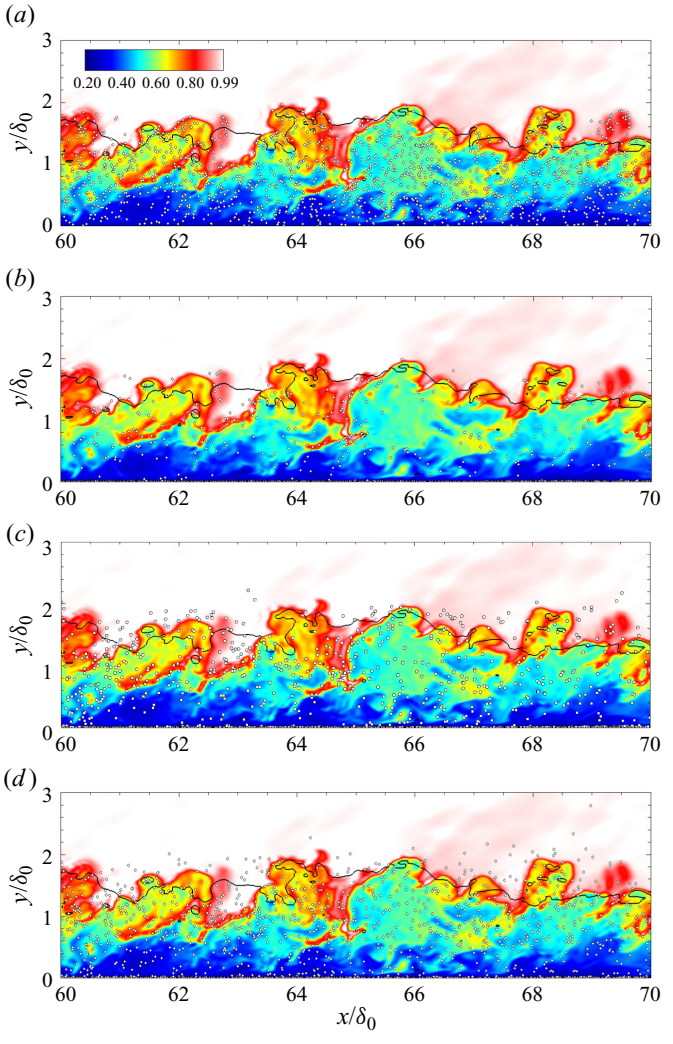

Figure 3. Instantaneous density distribution at $z = 0$ (flooded) and particles within $z = 0$–$0.01\delta_0$ in case M4, for particle populations (*a*) P1, (*b*) P4, (*c*) P5, (*d*) P6. Black solid lines indicate $u_1 = 0.99U_\infty$.

identical expression of (3.1) and the continuity equation. It is therefore reasonable that the density and the low Stokes number particle concentration fields are similar, except that there are mean gradients in the fluid density due to the restriction of the state equation of the perfect gas and the non-uniformity of the mean temperature in the wall-normal direction.

To further characterize the wall-normal transport of the particles, in figure 4 we present the wall-normal velocity of the fluid and the in-plane particle velocity vectors. For population P1, the wall-normal velocities of these low Stokes number particles follow almost exactly that of the fluid, in that the particles are moving upwards in the regions of ejections and downwards in the regions of sweeps within the boundary layer. However, near the edge of the boundary layer, the particles prefer to accumulate by the strong ejections, as suggested by higher particle concentration within the regions of positive wall-normal velocity $u_2 > 0$ compared to those of the negative wall-normal velocity

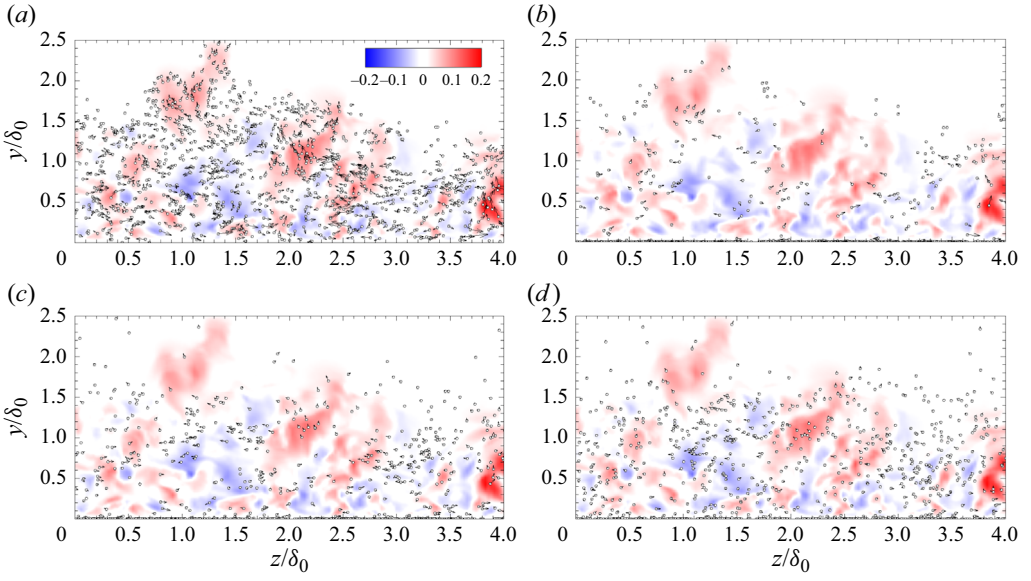

Figure 4. Instantaneous wall-normal velocity of the fluid u_2 (flooded) at $x = 60\delta_0$ and particle distribution within $x = (60–60.01)\delta_0$ in case M4, for (*a*) P1, (*b*) P4, (*c*) P5, (*d*) P6. Arrows indicate in-plane particle velocity vectors.

$u_2 < 0$. This has been examined via probability density distributions, as demonstrated in Appendix C. A simple reason is that there is no particle outside the boundary layers, so no particle can be brought downwards into the turbulent boundary layers from the free stream flow. This will be reflected in the statistics of particles as well, as will be shown subsequently. As for the other particle populations with larger Stokes numbers St^+, their wall-normal transport processes are still approximately following those of the fluid, while the magnitudes are reduced due to the larger particle inertia. In spite of this, the particles are more inclined to move outwards to the free stream, even inside $u_2 < 0$ regions, which is probably the remnant of the strong ejection events or equivalently the historical effects of the large-inertia particles (Soldati 2005). However, it should be noted that the number of particles escaping the turbulent boundary layers does not increase monotonically with the Stokes number. On the one hand, it can be derived that in the comparatively quiescent flow, the initial slip velocity required for the particles to reach the free stream is proportional to the reciprocal of the Stokes number. Henceforth, the high Stokes number particles are capable of escaping the boundary layers even though their wall-normal velocities are generally small. On the other hand, the bursting events endowed with high-intensity vertical momentum are usually short-lived (Tardu 1995; Jiménez 2013, 2018), so it is unlikely that the extremely high Stokes number particles can be accelerated to the threshold of escaping the boundary layer. Subject to these counteracting factors, the number of particles reaching the free stream should be first increasing then diminished, and when the Stokes numbers are sufficiently large, recovers to zero, for the particles will remain an almost straight trajectory with slight influences by the turbulent motions.

In figure 5, we present the distribution of the streamwise velocity fluctuation u_1' at $y^+ = 15$ and the particles within the range $y^+ = 3–15$. As is commonly observed in dilute multi-phase wall turbulence (Rouson & Eaton 2001; Sardina *et al.* 2012; Bernardini *et al.* 2013), the particles with low St^+ are evenly distributed in the wall-parallel plane,

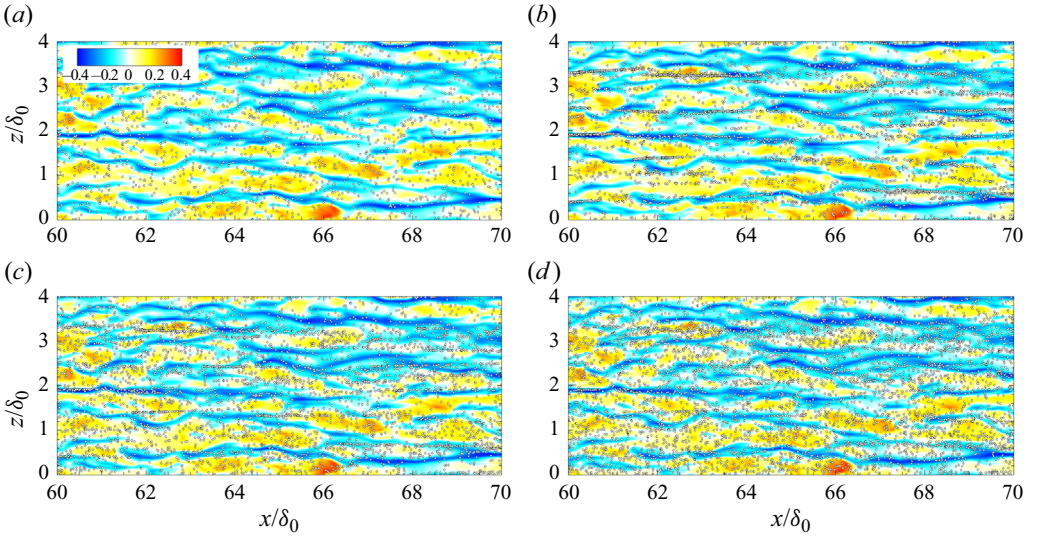

Figure 5. Instantaneous streamwise velocity fluctuation u_1' at $y^+ = 15$ (flooded) and particle distribution within $y^+ = 3$–15 in case M4, for (*a*) P1, (*b*) P4, (*c*) P5, (*d*) P6.

while their clustering with the low-speed streaks can be spotted for moderate St^+ particles (populations P4 and P5), which is induced by the near-wall quasi-streamwise vortices that transport the particles towards the viscous sublayer and are deposited by the spanwise velocity below the low-speed streaks, where they are either trapped or brought upwards when encountered with the strong ejections (Marchioli & Soldati 2002; Soldati & Marchioli 2009). At larger St^+ in type P6, the 'particle streaks' are weakened, showing a more uniform distribution, which is caused by the highly different particle response time and characteristic time scale of the near-wall self-sustaining cycle. Much longer particle streaks with wider spanwise intervals will be observed in high Reynolds number flows in which the very-large-scale motions are becoming more and more manifest, and contribute significantly to the Reynolds stress (Jie *et al.* 2022; Motoori *et al.* 2022).

3.2. *Near-wall accumulation and clustering*

The non-uniform wall-normal distribution can be characterized quantitatively by the mean particle concentration, calculated based on the grid centre of the Eulerian frame as

$$c(y_j) = \frac{N_p(y_j)}{\sum_j N_p(y_j)} \frac{\sum_j \Delta h_j}{\Delta h_j}, \quad j = 1, 2, \ldots, N_y - 1, \tag{3.2}$$

where $N_p(y_j)$ is the particle number located between the jth and $(j+1)$th grid points, and Δh_j is the grid interval. The distributions of the mean particle concentration $\bar{c}(y)/c_0$ are displayed in figures 6(*a–c*), with c_0 the particle concentration in the case of the perfect uniform wall-normal distribution. In general, the particles are almost evenly distributed across the boundary layer for the populations with the lowest Stokes number St^+, and the phenomenon of the near-wall accumulation, namely the turbophoresis, becomes more evident with increasing St^+. The maximal near-wall particle number density is attained for the particle type P4, beyond which it is gradually diminished. This is consistent with the

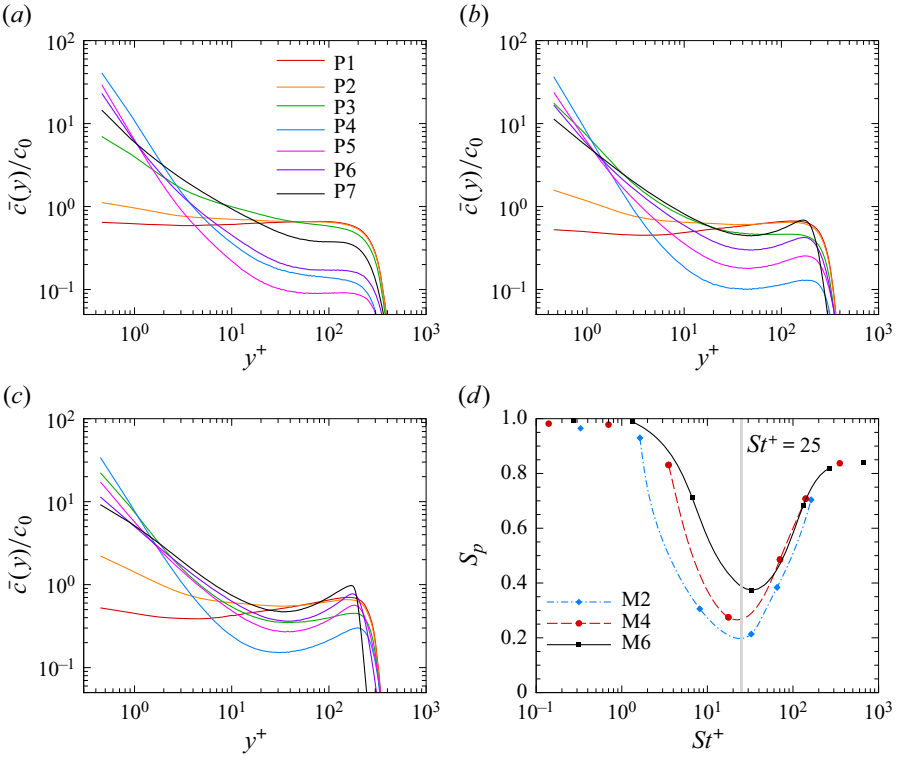

Figure 6. Wall-normal distribution of the particle concentration in cases (*a*) M2, (*b*) M4 and (*c*) M6; and (*d*) the Shannon entropy at different Stokes numbers St^+ at $t = 515\delta_0/U_\infty$. Lines in (*d*) are the cubic splines using the data within $St^+ = 1$–300.

conclusions in low-speed turbulent channel flows (Sardina *et al.* 2012; Bernardini 2014). Comparing these cases, we found that the particle concentrations $\bar{c}(y)$ within the range $y^+ = 50$–200 remain almost constant in case M2, whereas those in cases M4 and M6 slightly increase and manifest secondary peaks in the outer region, especially for the large St^+ particle populations. Such non-monotonic variations are probably caused by the evident variation of the particle Stokes number St^* at high Mach numbers when evaluated by the local density and viscosity of the fluid.

A commonly used indicator of the non-uniform wall-normal distribution is the Shannon entropy (Picano, Sardina & Casciola 2009). It is defined by the ratio of two entropy parameters, $S_p = \mathscr{S}/\mathscr{S}_{max}$, in which $\mathscr{S}$ is calculated in equidistant slabs in the wall-normal direction within 1.2δ:

$$\mathscr{S} = -\sum_{j=1}^{N_{yu}} P_j \ln(P_j), \tag{3.3}$$

with $N_{yu} = 200$, and P_j the probability of finding a particle in the jth slab. In the case of evenly distributed particles, $\mathscr{S}$ attains a maximum $\mathscr{S}_{max} = \ln N_{yu}$. The Shannon entropy S_p therefore ranges from 0 to 1. In figure 6(*d*), we plot the values of S_p of each particle population in all three cases against St^+. As expected, the values of S_p are close to unity for low Stokes number particles, corresponding to the uniform distribution across the boundary layer, and decrease rapidly and attain a minimum at $St^+ \approx 30$ for all the

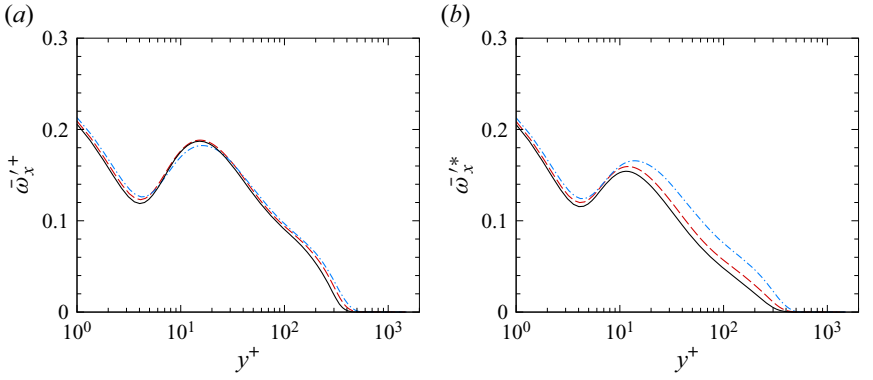

Figure 7. Wall-normal distribution of the streamwise vorticity fluctuation root mean square, normalized by (*a*) viscous scale δ_ν/u_τ, $\bar{\omega}_x'^+$, (*b*) local viscous scales δ_ν^*/u_τ^*, $\bar{\omega}_x'^*$. Blue dash-dotted lines indicate case M2; red dashed lines indicate case M4; black solid lines indicate case M6.

cases considered, irrespective of the free stream Mach numbers, suggesting the highest level of near-wall accumulation. This is consistent with previous studies on particles in incompressible turbulent channels (Marchioli & Soldati 2002; Bernardini 2014). For particles with St^+ greater than 300, the S_p values tend to reach an asymptotic value 0.85, implying that the tendency of near-wall accumulation of particles remains even when the particles respond to the turbulent motions rather slowly, which is probably caused by the integral effects of their remaining inside the turbulent boundary layer. Comparing the cases at different Mach numbers, we further found that the higher Mach numbers tend to alleviate the turbophoresis phenomenon. This can be inferred from the larger particle number density near the edge of the boundary layer. It is reminiscent of the higher particle concentration near the channel centre within the quiescent cores (Jie *et al.* 2021) and the free surface of the open channel (Yu *et al.* 2017; Gao, Samtaney & Richter 2023), which was attributed to the corresponding lower turbulent intensities (Mortimer & Fairweather 2020). Such a phenomenon is found to be more evident for larger Stokes number particles. Therefore, the more intense particle concentration near the edge of the boundary layer with increasing Mach number should probably be attributed to the larger St^*, as reported in figure 2(*d*).

Since the near-wall accumulation is related mainly to the ejection and sweeping events induced by the quasi-streamwise vortices (Marchioli & Soldati 2002; Soldati & Marchioli 2009), the dependence of the Shannon entropy on the Mach number is probably caused by the variation of the characteristics of the streamwise vortices. In figure 7, we present the root mean square (RMS) of the streamwise vorticity fluctuations, $\bar{\omega}_x'$, normalized by the viscous scales and local viscous scales, respectively. For the local peaks at $y^+ \approx 10$–20 that represent the average intensity of the quasi-streamwise vortices, the former shows weak dependence on the Mach number, while the latter manifests a systematic decreasing trend of variation. From another point of view, the normalization using the viscous scales is more of a kinetic description of the fluid motions, while that using the local viscous scales incorporates the variation of the fluid density and viscosity that influence the motions of the particles. Therefore, we conclude that the decreasing $\bar{\omega}_x'^*$ suggests the weaker impacts of the streamwise vortices on the near-wall particle motions, consistent with the observations of the less intensified near-wall accumulation with the Mach number.

Besides the near-wall accumulation, another crucial aspect of the particle organization in wall turbulence is the clustering behaviour in the wall-parallel planes induced by the turbulent structures. Amongst the multiple methods of quantifying such a phenomenon, such as the maximum deviation from randomness or the segregation parameter (Fessler, Kulick & Eaton 1994; Picciotto *et al.* 2005*b*), the scaling of the radial distribution function (RDF) (Wang & Maxey 1993; Pumir & Wilkinson 2016), the statistics of particle concentration and the Voronoï tessellation analysis (Monchaux, Bourgoin & Cartellier 2010, 2012), we adopt the angular distribution function (ADF) proposed by Gualtieri, Picano & Casciola (2009), which has been applied to turbulent channel flows in Sardina *et al.* (2012) for the characterization of the inhomogeneous near-wall particle organization. Following Sardina *et al.* (2012), we define the two-dimensional ADF as

$$g(r,\theta) = \frac{1}{r}\frac{\mathrm{d}\nu_r}{\mathrm{d}r}\frac{1}{n_0(y)}, \tag{3.4}$$

with r the wall-parallel inter-particle distance, θ the deviation angle from the x direction, $\nu_r(r,\theta)$ the averaged particle pair number at a certain off-wall distance y, and n_0 the total number of particle pairs per unit area obtained by

$$n_0(y) = \frac{1}{2A}N_p(y)\,(N_p(y)-1), \tag{3.5}$$

where A is the wall-parallel area where the statistics are performed.

In figure 8, we present the ADF distributions for particle populations P2 to P7 in case M4. The trend of variation is qualitatively consistent with that in low-speed turbulent channels (Sardina *et al.* 2012). Specifically, the particle population P2 with St^+ closest to unity manifests the weakest degree of small-scale clustering and the general uniform distribution, as indicated by the merely slightly higher value of ADF at $r=0$ compared to those away from it, where they remain almost constant. For particle populations P3 to P5 with the gradually larger St^+, the probability of finding particles adjacent to them in the streamwise direction is higher, corresponding to the formation and the more evident streamwise elongated particle streaks. At the even larger St^+ for particle populations P6 and P7, the particle streaks still exist but become less evident due to the higher probability away from $l_z^+=0$. This is consistent with the observations in figure 5 that the particles tend to be uniformly distributed when their inertia is large.

Integrating the ADF in the azimuthal direction, we can obtain its isotropic component without incorporating the directional variation, namely the RDF

$$g_0(r) = \frac{1}{2\pi}\int_0^{2\pi} g(r,\theta)\,\mathrm{d}\theta. \tag{3.6}$$

The results for cases M2, M4 and M6 are shown in figures 9(*a–c*). Here, $g_0(r)$ characterizes the probability of finding particle pairs within the circle of radius r, suggesting the level of radial particle clustering. For the presently considered cases, particle populations P4 and P5 show the most evident tendency for clustering, while for the other particle populations, such an effect is alleviated. Comparing these cases, we found that the particles with the highest value of $g_0(r)$ at the limit $r\to 0$ share approximately the same particle inertia under wall viscous units, $St^+\approx 15$–50.

The RDF $g_0(r)$ is capable of reflecting the small-scale clustering (Bec *et al.* 2007; Saw *et al.* 2008), as suggested by its association with the number of particle pairs within

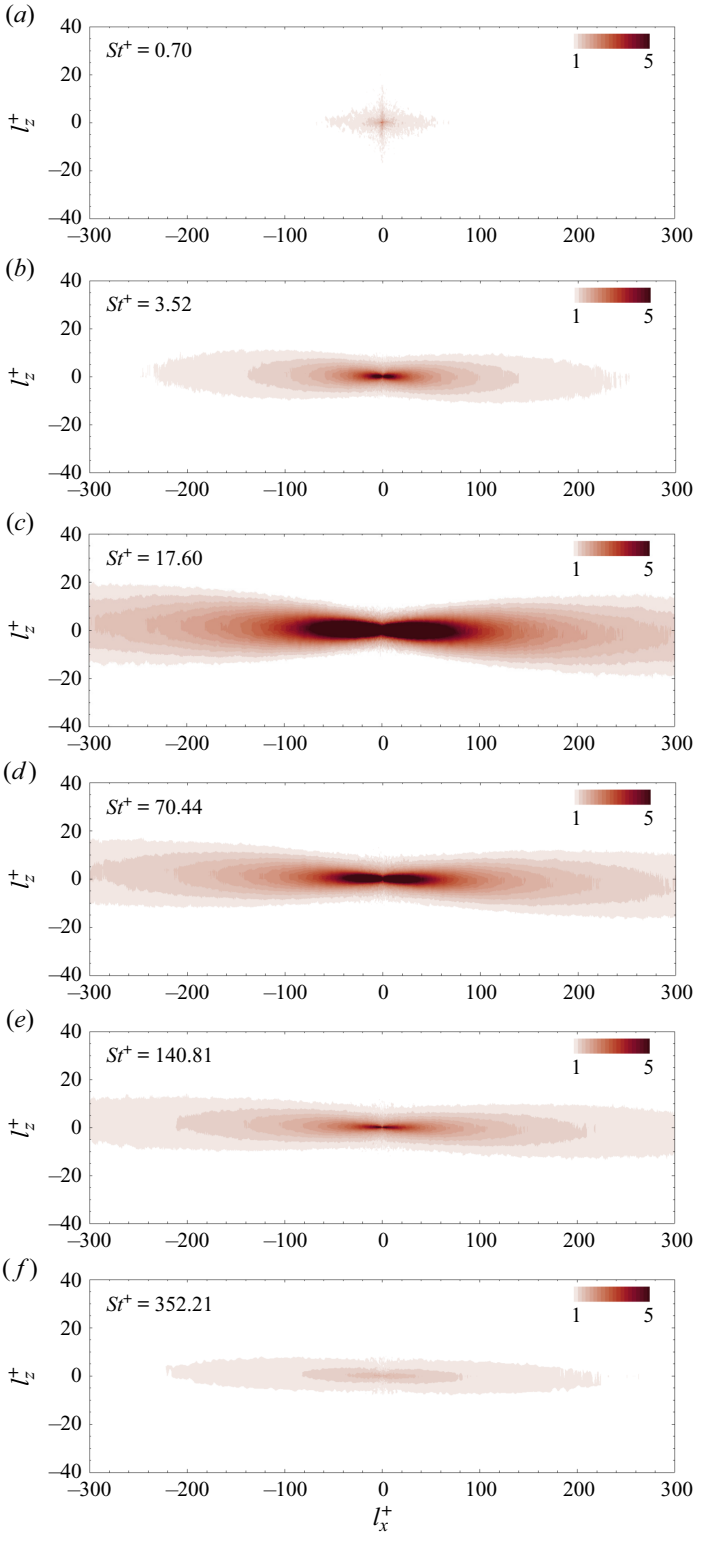

Figure 8. Near-wall particle angular distribution function below $y^+ = 10$ of case M4, for (*a*) P2, (*b*) P3, (*c*) P4, (*d*) P5, (*e*) P6, (*f*) P7.

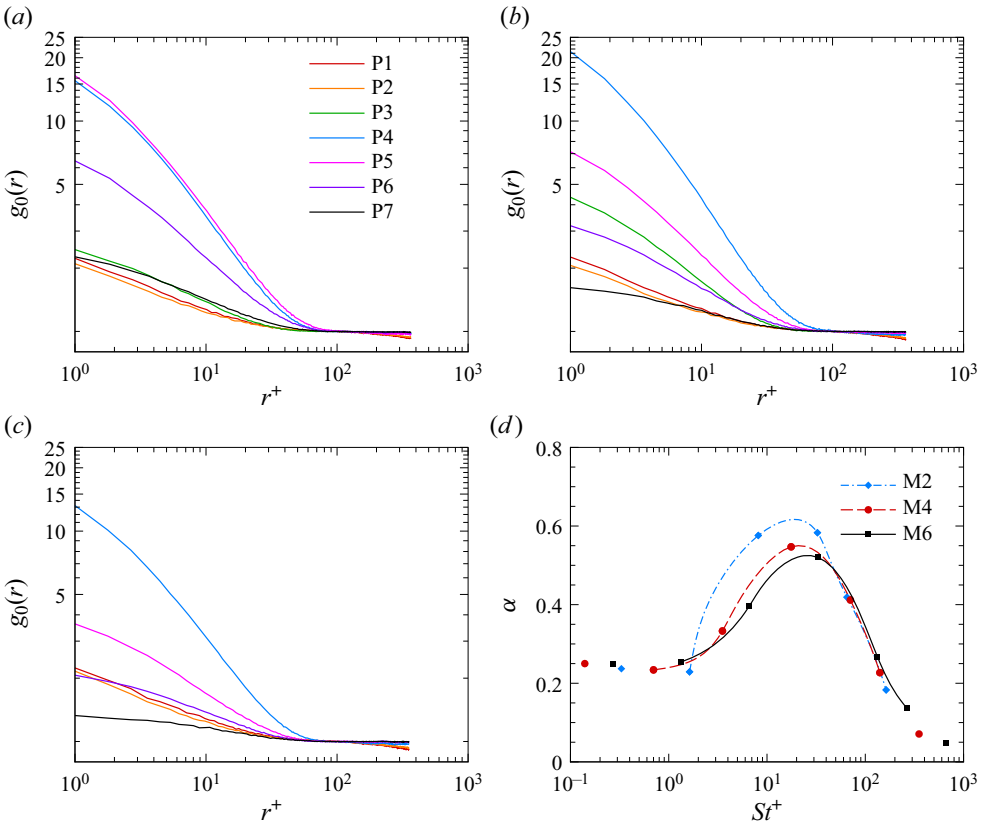

Figure 9. Isotropic component of the ADF $g_0(r)$ below $y^+ = 10$, for (*a*) case M2, (*b*) case M4, (*c*) case M6; and (*d*) power law of $g_0(r)$ at $r \to 0$ against St^+.

radius r:

$$\mathcal{N}(r) = n_0 \int_0^{2\pi} \int_0^r r'\, g(r', \theta)\, \mathrm{d}r\, \mathrm{d}\theta. \tag{3.7}$$

For the spatially uniformly distributed particles, $\mathcal{N}(r)$ can be estimated as $\mathcal{N}(r) = n_0(y)\, \pi r^2$, hence g_0 being constant, otherwise the decay of g_0 at the limit $r \to 0$ should follow $g_0 \propto r^{-\alpha}$ with $\alpha > 0$. The exponents α in the power law for all the particle populations in each case are shown in figure 9(*d*), with cubic spline curve fitting using the data within the range $St^+ = 5$–300. It can be observed that the peaks of α are attained at $St^+ \approx 15$–30, and the tendency of small-scale clustering is mitigated by the higher Mach number. This is probably caused by the lower level of the near-wall particle accumulation at higher Mach numbers, which reduces the particle numbers close to the wall (figure 6*d*).

The anisotropy indicator of the particle clustering can be obtained by the ADF as (Casciola *et al.* 2007; Sardina *et al.* 2012)

$$A(r) = \sqrt{\frac{\int (g(r, \theta) - g_0(r))^2\, \mathrm{d}\theta}{\int g_0^2(r)\, \mathrm{d}\theta}}, \tag{3.8}$$

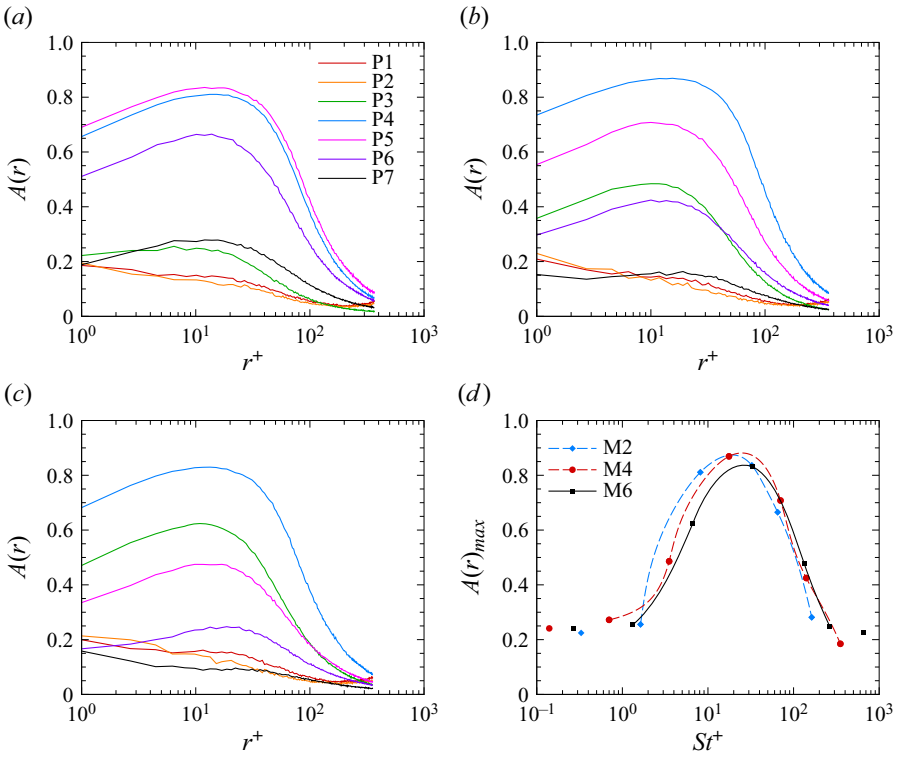

Figure 10. Anisotropy indicator $A(r)$ of the ADF below $y^+ = 10$, for (*a*) case M2, (*b*) case M4, (*c*) case M6; (*d*) the maxima of $A(r)$ against St^+.

indicating the directional non-homogeneity of the wall-parallel particle distribution. The results are shown in figures 10(*a–c*). For particles with small St^+ or those with St^+ greater than 200, the values of $A(r)$ are small and decay almost monotonically with increasing r^+, suggesting the weak directional dependence of $g(r, \theta)$ and hence the uniform distribution in almost all directions. For other particle populations with St^+ ranging from 5.0 to 200, the levels of $A(r)$ are higher, and the peaks are attained not at the limit $r^+ \to 0$, but at a finite $r^+ = 10$–20, especially for particle population P4, which displays a high level of spatial non-homogeneity for all the cases considered. This implies that the narrow streaky structures with the width $(20–40)\delta_\nu$, which is in accordance with the spanwise scale of the low-speed streaks. (The characteristic spanwise length scale $\lambda_z^+ \approx 100$ read from the spectra of Hwang (2013) is the averaged spanwise intervals between the two streaks. The low-speed streaks are narrower than the high-speed ones, as suggested by the conditional average reported by Wang, Huang & Xu 2015.) For the purpose of comparison between cases with different Mach numbers, in figure 10(*d*) we plot the maximum of $A(r)$ against St^+. Note that only the maxima of $A(r)$ in particle populations P3 to P6 are attained at non-zero r. The level of clustering with the velocity streaks does not manifest significant variation in different cases, further suggesting the weak dependence on the Mach number of the near-wall fluid and particle dynamics. Moreover, this trend of variation is similar to the near-wall accumulation discussed in figure 6. In fact, it has been observed previously that the near-wall accumulation and the clustering are two different aspects of the same process (Sardina *et al.* 2012): that the near-wall streamwise vortices bring the high Stokes

number particles towards the near-wall regions where they reside for a rather long period, during which they are shifted horizontally to the low-speed streaks (Soldati & Marchioli 2009), thereby leading to the coexistence of the two phenomena.

In this section, we have presented the instantaneous and statistical organizations of the particles with different inertia at various Mach numbers. We found that the instantaneous distributions of the low Stokes number particles are similar to those of the fluid density, restrained within the turbulent boundary layer, while the high Stokes number particles are capable of escaping the turbulent region and reaching the free stream. The ubiquitous near-wall accumulation and the clustering phenomena in low-speed flows are observed in the high-speed flows considered herein, with the former slightly weakened with increasing Mach number.

4. Particle dynamics

In this section, we will further discuss the kinematics and dynamics of particles, including their mean and fluctuating velocity and acceleration, with a special focus on the effects of the particle inertia at various Mach numbers.

4.1. *Mean and fluctuating particle velocity*

In figure 11, we present the wall-normal distributions of the streamwise and wall-normal mean fluid velocity seen by particles $\bar{u}_{i,p}$ and the mean particle velocity $\bar{v}_i$ in case M4, with the other cases omitted here due to the similar conclusions to be drawn. In the streamwise direction,the mean fluid velocity seen by particles $\bar{u}_{1,p}$ (figure 11*a*) is well-collapsed with the mean velocity $\bar{u}_1$, except for the lower values for the particle population P4, which show the most evident clustering beneath the low-speed streaks (Narayanan *et al.* 2003; Xiao *et al.* 2020). The statistics of particle populations with lower and higher Stokes numbers do not show such discrepancies from the mean fluid velocity $\bar{u}_1$ because of their comparatively uniform distributions. The mean streamwise particle velocity $\bar{v}_1$ (figure 11*b*) behaves differently. The $\bar{v}_1$ values of the low Stokes number particle populations (P1 and P2) are in general consistency with the mean fluid velocity $\bar{u}_1$. As St^+ increases to moderate values (P3 and P4), the mean particle velocities $\bar{v}_1$ are lower than that of the fluid $\bar{u}_1$ in the buffer region, but recover as it reaches $y^+ \gtrsim 60$. For high Stokes number particle populations P5, P6 and P7, the $\bar{v}_1$ values are higher than the mean fluid velocity beneath $y^+ \approx 10$, and lower above that location. These phenomena should be caused by the tendency to their increasing tardiness of being accelerated or decelerated because of their comparatively larger inertia, especially for particle populations P5 to P7. Since they are not bounded by the no-slipping velocity condition at the wall, these high Stokes number particles either keep rolling on the wall before they are erupted or decelerated to zero velocity or reflected away from the wall (Picciotto *et al.* 2005*a*; Mortimer *et al.* 2019). As a result, the mean velocity profiles of the particles are consistently flatter than those of the fluid (Kulick, Fessler & Eaton 1994).

The wall-normal velocities, on the other hand, show some peculiar phenomena. Although small in value, $\bar{u}_{2,p}$ (figure 11*c*) is higher than the mean fluid velocity $\bar{u}_2$ across the boundary layer, even for the small particles. Since the particle populations with moderate and large St^+ (P3 to P7) tend to accumulate within the low-speed regions, which are highly correlated with ejection events, the fluid velocity seen by particles, $\bar{u}_{2,p}$, is higher within $y^+ = 50$, with the highest values attained for particles in P4 and P5 that show the most significant clustering behaviour (Soldati & Marchioli 2009; Zhao *et al.* 2012;

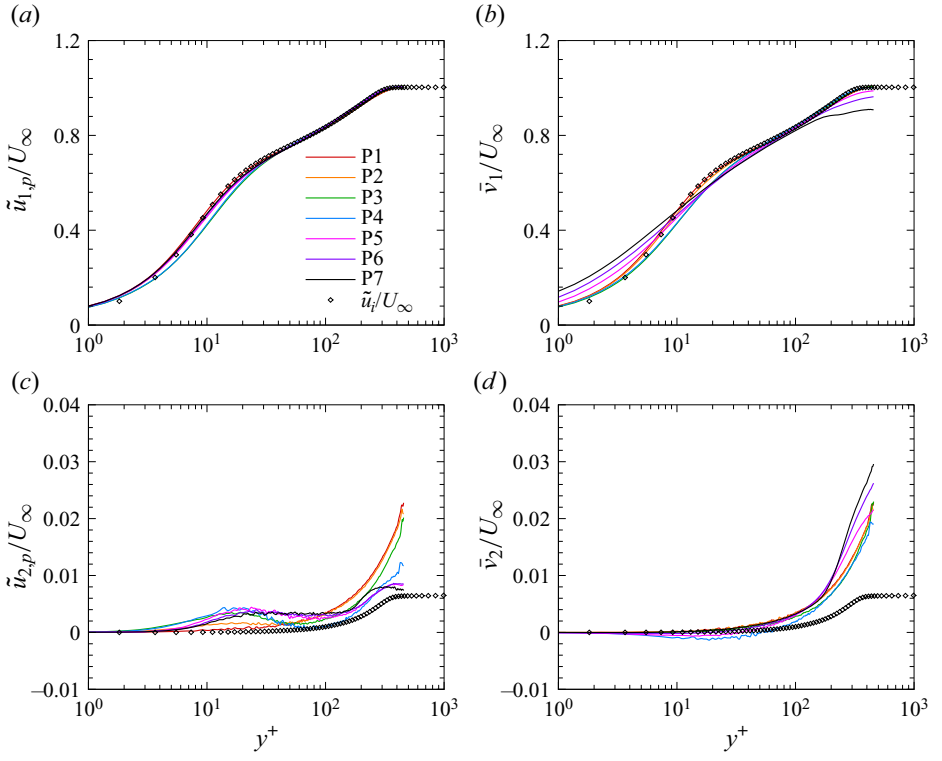

Figure 11. Mean velocity of (*a*,*c*) fluid seen by particles $\bar{u}_{i,p}$, and (*b*,*d*) particles $\bar{v}_i$ in the (*a*,*b*) streamwise and (*c*,*d*) wall-normal directions, in case M4.

Milici & de Marchis 2016). In the outer region, however, the trend is reversed. We can attribute such a trend of variation to the fact that the low Stokes number particles are restrained within the boundary layers so that only the ejections can be reflected in $\bar{u}_{2,p}$, whereas the high Stokes number particles are capable of escaping towards the free stream, thus alleviating the high $\bar{u}_{2,p}$ values. The mean particle velocities $\bar{v}_2$ (figure 11*d*) close to the wall are approximately zero, while they are higher than the mean fluid velocity $\bar{u}_2$ above $y^+ = 50$ and than that seen by particles $\bar{u}_{2,p}$ in the outer region for all particle populations, showing weak dependence on the particle inertia. Similar results have been reported by Xiao *et al.* (2020) at the free stream Mach number 2.0 for particles with $St^+ = 2.36$ and 24.33. This suggests that the mean particle wall-normal velocities are probably merely associated with the spatial development of the boundary layer.

In figure 12, we present the RMS of the streamwise and wall-normal components of the particle velocity fluctuations, denoted as $\bar{v}_i'$. The trend of variation is in general agreement with that in incompressible turbulent channel flows (Marchioli *et al.* 2008; Vinkovic *et al.* 2011; Li, Wei & Yu 2016; Fong, Amili & Coletti 2019). Specifically, within the boundary layer, the RMS of the low Stokes number particles (P1 and P2) are well-collapsed with those of the fluid. The peaks of $\bar{v}_1'$ vary non-monotonically with the increasing St^+, shifting gradually towards the wall, showing no tendency to decrease to zero near the wall. In the outer region, the $\bar{v}_1'$ values are almost collapsed, manifesting weak dependence on the Mach number. The $\bar{v}_2'$ values, on the other hand, decrease monotonically with St^+. Besides these consistencies, there are two aspects that cannot be covered by the

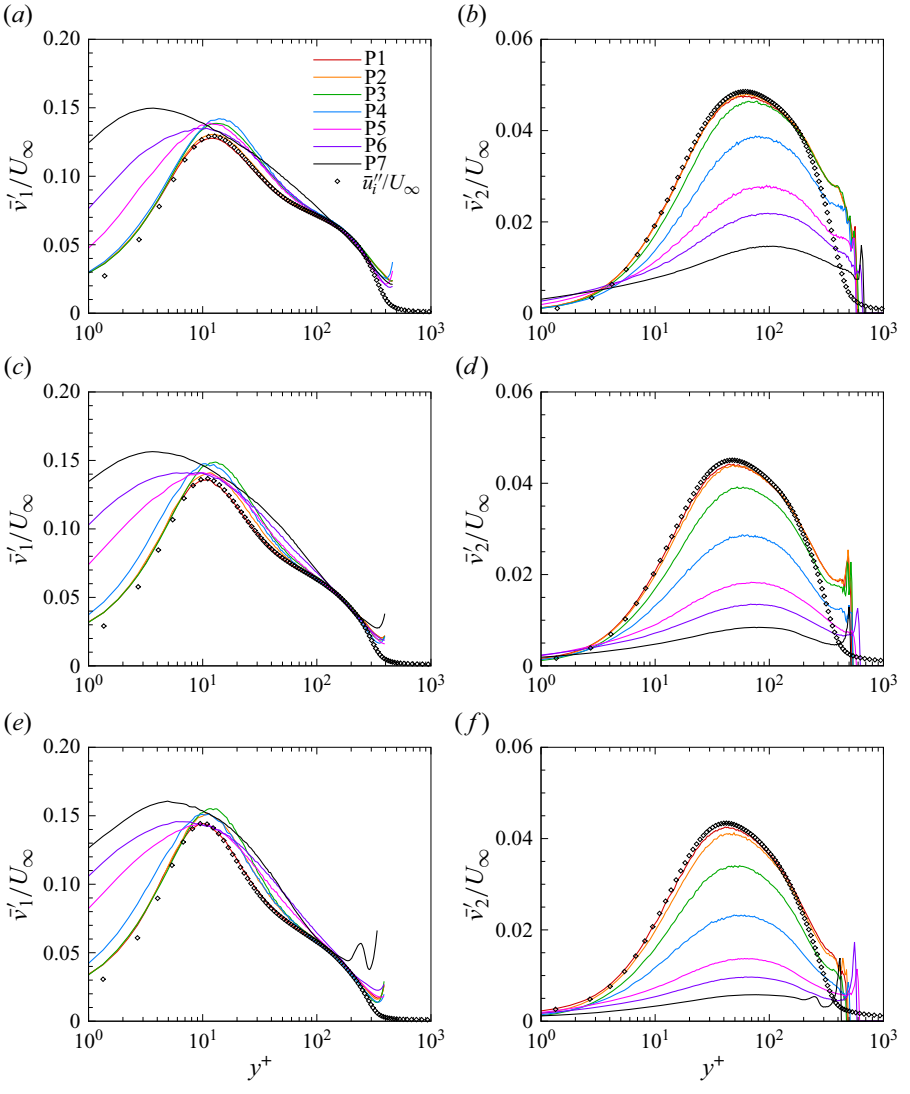

Figure 12. The RMS of particle velocity fluctuation: (*a*,*c*,*e*) $\bar{v}_1'$, (*b*,*d*,*f*) $\bar{v}_2'$, in (*a*,*b*) case M2, (*c*,*d*) case M4, and (*e*,*f*) case M6.

observations of previous studies. First, if we plot the near-wall local maximum of $\bar{v}_1'$ against the Stokes number St^+, as displayed in figure 13(*a*), we find that the former is not varying monotonically with the latter, with local maxima achieved at $St^+ \approx 10$ for each case but showing consistent decrement with the increasing Mach number. The peaks of $\bar{v}_2'$ compared with those of the fluid (figure 13*b*), however, decrease systematically, with very weak Mach number effects. The differences in the $\bar{v}_1'$ values in various cases are probably ascribed to the variation of the particle Mach number that is related to the drag force acting on the particles, which will be discussed in the next subsection. Second, both $\bar{v}_1'$ and $\bar{v}_2'$ deviate from the RMS of fluid velocity fluctuation near the edge of the boundary layer, even at the lowest St^+. This is beyond expectation, because these low Stokes number particles, which are commonly used in experimental measurements to obtain velocity in

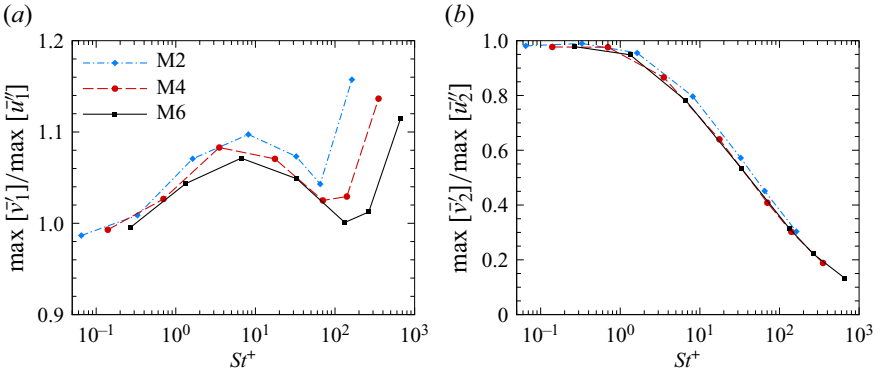

Figure 13. Ratio between the peak values of $\bar{v}_i'$ in the near-wall region and $\bar{u}_i''$ for different cases, for components (*a*) $\bar{v}_1'$ and (*b*) $\bar{v}_2'$.

such methods as particle image velocimetry, should be capable of following the trajectories and replicating the statistics. The reason is similar to the higher $\bar{v}_2$ and $\bar{u}_{2,p}$ compared with $\bar{u}_2$. Considering the numerical settings in the present study, the particles with small St^+ are primarily restricted beneath the turbulent–non-turbulent interfaces, thereby reflecting only the statistics in the turbulent region but avoiding those in the non-turbulent region and hence the higher intensities. Such a bias will be amended if the particles at the inlet are statistically uniformly distributed within a region much higher than the nominal boundary layer thickness. We have performed extra simulations for the verification of this inference, details of which can be found in Appendix D.

4.2. *Particle acceleration*

Equation (2.10) dictates that the forces acting on the particles, or equivalently the particle accelerations, are related to the slip velocity, particle inertia and particle Reynolds and Mach numbers, which will be presented in detail subsequently.

We first consider the slip velocity, namely the difference between the fluid and particle velocities $u_i - v_i$. The mean slip velocity is equivalent to the difference between the mean particle velocity $\bar{v}_i$ and the mean fluid velocity seen by particles $\bar{u}_{i,p}$. In figure 14, we present the distribution of $\bar{v}_{i,s}$ across the boundary layer. The statistics are qualitatively consistent with those in incompressible turbulent channel flows in the near-wall region (Zhao *et al.* 2012), but are different in the outer region. In the streamwise direction, the particles incline to move faster than the fluid in the near-wall region below $y^+ \approx 10$, but slower above that location. The non-zero slip mean velocities close to the wall suggest that the particles are capable of sliding horizontally near the wall. The magnitudes of the peaks and valleys increase monotonically with the Stokes number. In the wall-normal direction, on the other hand, the slip velocity $\bar{v}_{2,s}$ is positive below $y^+ = 100$, while it is negative above it. The peaks of $\bar{v}_{2,s}$ are attained at $y^+ \approx 20$, manifesting a non-monotonic variation and reaching a maximum for particle population P4 in case M2, and P5 in cases M4 and M6 that show the utmost near-wall accumulation. This indicates that the particles either move much faster towards or slower away from the wall, leading to the gradually increasing numbers of particles in the near-wall region. In the outer region, the particles tend to move faster than the fluid to the free stream, or slower when re-entrained within the boundary layer, consistent with the observation in the instantaneous flow fields (figure 3) that the particles with large inertia are capable of escaping the turbulent region.

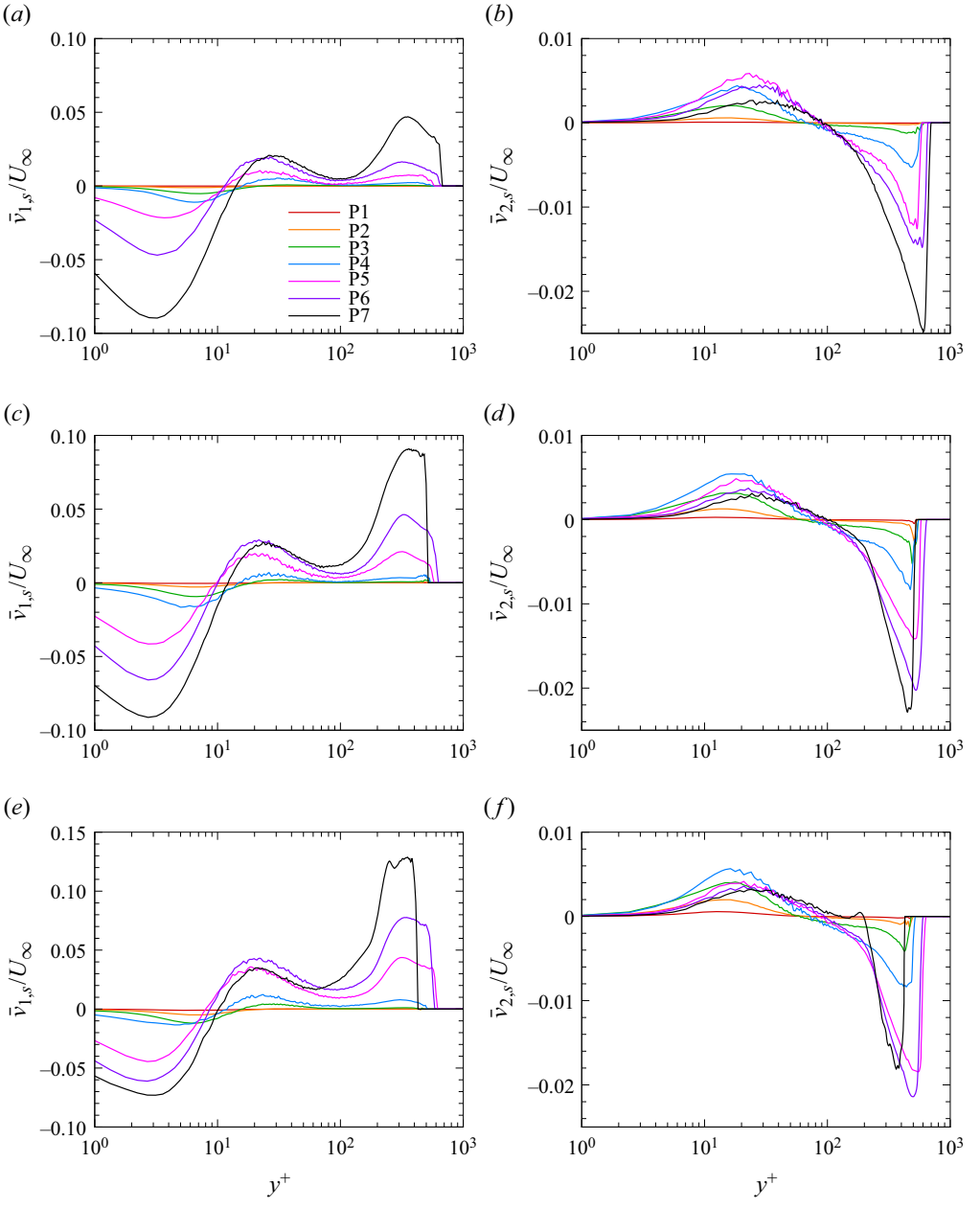

Figure 14. Mean particle slip velocity (*a*,*c*,*e*) $\bar{v}_{1,s}/U_\infty$, (*b*,*d*,*f*) $\bar{v}_{2,s}/U_\infty$, in cases (*a*,*b*) M2, (*c*,*d*) M4 and (*e*,*f*) M6.

In figure 15, we present the RMS of the slip velocity, represented by $\bar{v}'_{i,s}$. In general, the distributions of $\bar{v}'_{i,s}$ resemble those of the velocity and become more intense with increasing St^+, except the non-zero values of $\bar{v}'_{i,s}$ close to the wall because of (as explained above) the different boundary conditions implemented on the fluid and particles, with the streamwise component $\bar{v}'_{1,s}$ related to the particle slipping near the wall and the wall-normal component $\bar{v}'_{2,s}$ to the particles hitting and/or bouncing off the wall. It is

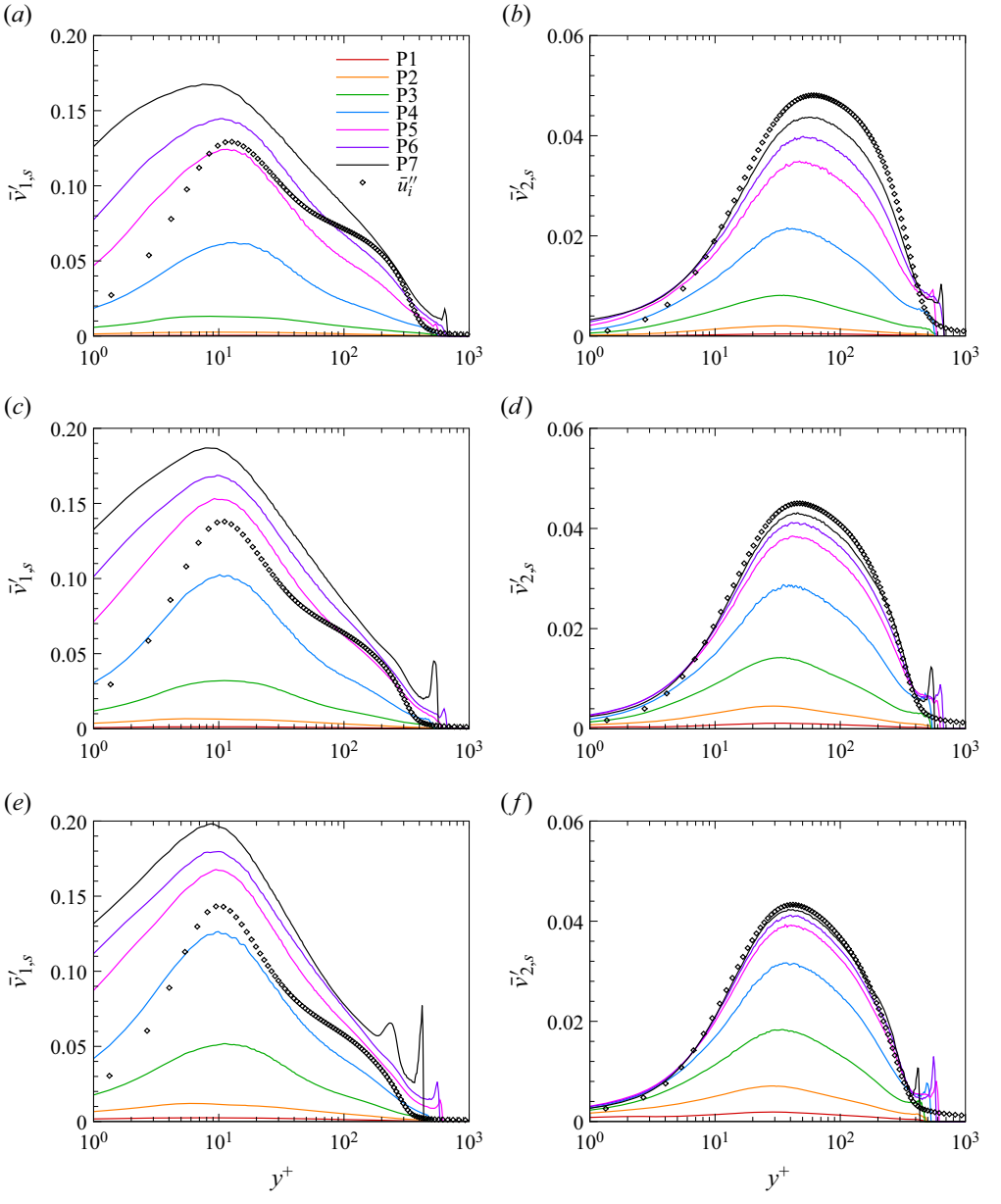

Figure 15. The RMS of particle slip velocity fluctuation (*a*,*c*,*e*) $\bar{v}'_{1,s}$, (*b*,*d*,*f*) $\bar{v}'_{2,s}$, for (*a*,*b*) case M2, (*c*,*d*) case M4, and (*e*,*f*) case M6.

interesting to note that $\bar{v}'_{1,s}$ values for larger inertia particle populations are higher than the corresponding velocity fluctuations, suggesting that the particle velocity fluctuations are frequently of opposite sign to that of the fluid. The $\bar{v}'_{2,s}$ values, on the other hand, are consistently lower than $\bar{u}'_2$, except for the small region near the edge of the boundary layer. Furthermore, we find that the maximum of $\bar{v}'_{1,s}$ and $\bar{v}'_{2,s}$ increases monotonically with St^+ (not shown here for brevity), irrelevant of the different free stream Mach numbers in these cases.

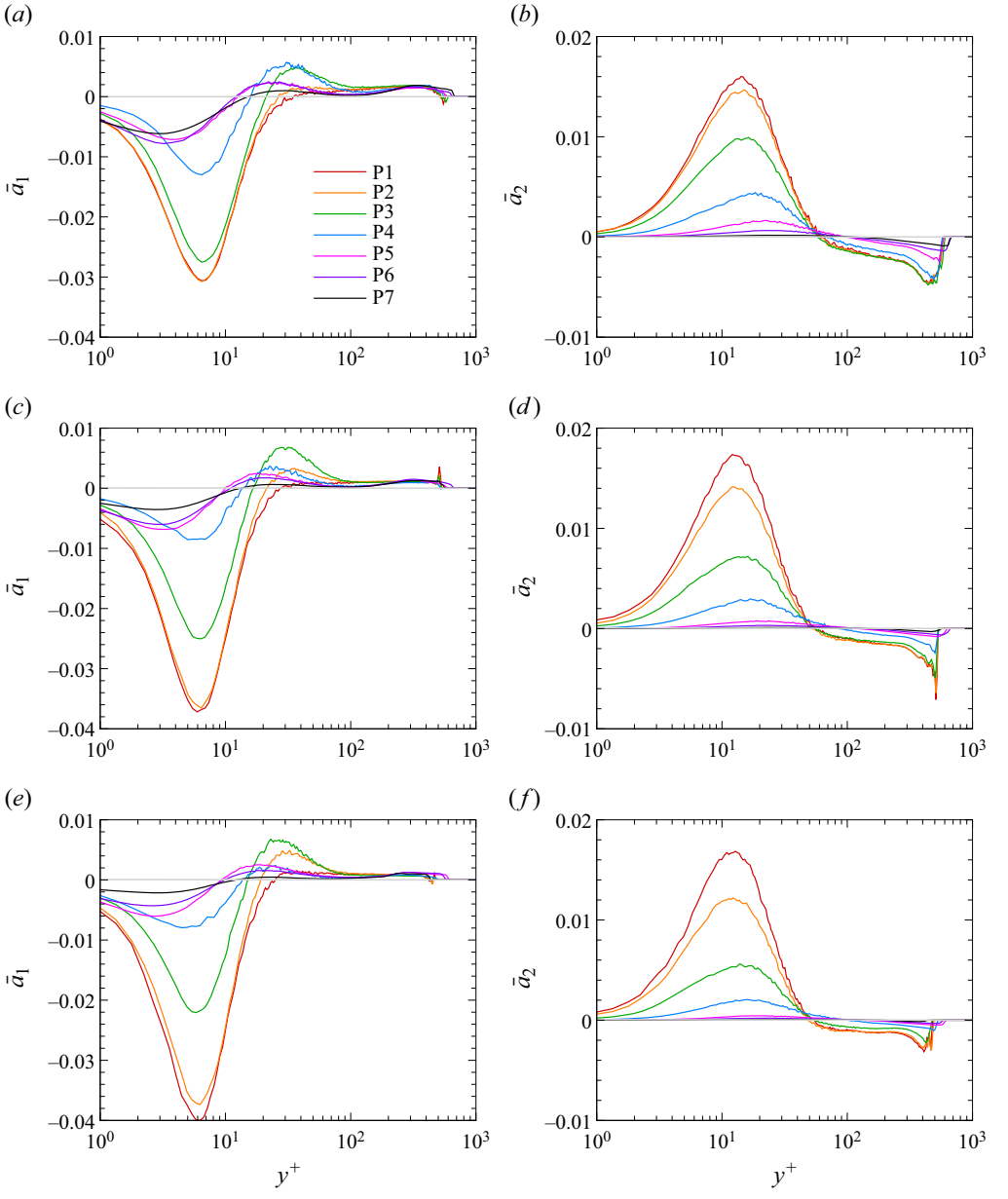

Figure 16. Mean particle acceleration, normalized by U_∞ and δ_0: (*a*,*c*,*e*) $\bar{a}_1$ and (*b*,*d*,*f*) $\bar{a}_2$, for (*a*,*b*) case M2, (*c*,*d*) case M4, and (*e*,*f*) case M6.

The slip velocity induces the forces on particles, resulting in their acceleration. Shown in figure 16 are their mean values in the streamwise and wall-normal directions. By comparing the distributions of the mean particle acceleration $\bar{a}_i$ for each case, we first find that the streamwise component $\bar{a}_1$ is negative in the near-wall region, and becomes positive above the buffer region, whereas the wall-normal component $\bar{a}_2$ manifests a reverse trend of variation. Second, both $\bar{a}_1$ and $\bar{a}_2$ possess higher magnitudes in the near-wall region, which is different from the mean slip velocities $\bar{v}_{i,s}$ for some of the

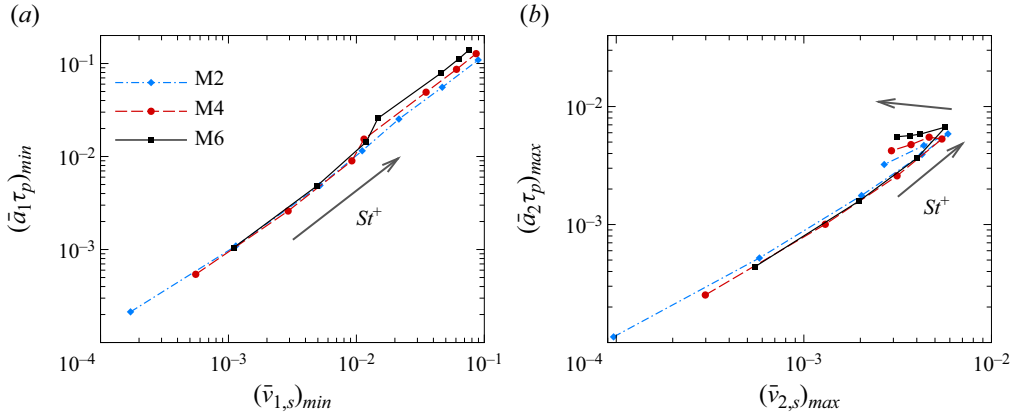

Figure 17. Relations between the mean acceleration and the mean slip velocity: (*a*) minimum of $\bar{v}_{1,s}$ and $\bar{a}_1\tau_p$; (*b*) maximum of $\bar{v}_{2,s}$ and $\bar{a}_2\tau_p$.

large-inertia particle populations. We can infer from (2.10) that the mean acceleration of the particles relies not only on the mean values of the slip velocity, but on their fluctuations and local viscosity as well. The fluctuations of the slip velocity are more intense in the near-wall region, and the local viscosity is lower away from the wall; both of these factors lead to the lower forces acting on the particles in the outer region. Third, the magnitudes of $\bar{a}_1$ and $\bar{a}_2$ decrease monotonically with increasing St^+ due to the increasing density of the particle populations, except for a thin layer in the buffer layer where the mean slip velocity $\bar{v}_{1,s}$ changes its sign. Knowing that the low-inertia particles follow the trajectories of the fluid, the distributions of the mean particle acceleration indicate that both the dispersed phase particle with low inertia and the fluid particles under the Lagrangian frame are decelerated in both the streamwise and wall-normal directions when they are swept downwards due to the restriction of the no-slip and no-penetration conditions imposed on the wall. As for high Stokes number particles, wall-normal mean acceleration $\bar{a}_2$ is almost zero, while the streamwise mean acceleration $\bar{a}_1$ retains finite values, suggesting that these particles, moving either towards or away from the wall, are barely or equally affected by the near-wall sweeping and ejection events, and can be accelerated or decelerated when they are travelling across the boundary layer due to the comparatively strong shear, in particular in the near-wall region.

Comparing these cases, however, it appears that the mean particle acceleration $\bar{a}_i$ does not obey a monotonic trend of variation with the Stokes number St^+, which is different from the other related flow quantities. In figure 17, we plot the minimum of $\bar{v}_{1,s}$ against that of $\bar{a}_1$, and the maximum of $\bar{v}_{2,s}$ against that of $\bar{a}_2$, with the acceleration multiplied by the particle relaxation time τ_p to incorporate the particle inertia. For particles with small St^+ (populations P1 to P3), the mean particle streamwise acceleration $\bar{a}_1\tau_p$ increases with the slip velocity almost linearly, and manifests no dependence on the free stream Mach number, as indicated by the well-collapsed profiles. The mean streamwise acceleration of high Stokes number particle populations, on the other hand, is stronger with increasing Mach number. The $\bar{a}_2\tau_p$ value does not increase monotonically with St^+ and, more importantly, it is greater for high Stokes number particle populations even when the mean slip velocities $\bar{v}_{2,s}$ are the same as those of the low Stokes number particle populations. According to (2.10), we deduce that the discrepancy in the trend of variation should be attributed to the function f_D that reflects the non-negligible effects of the particle Reynolds

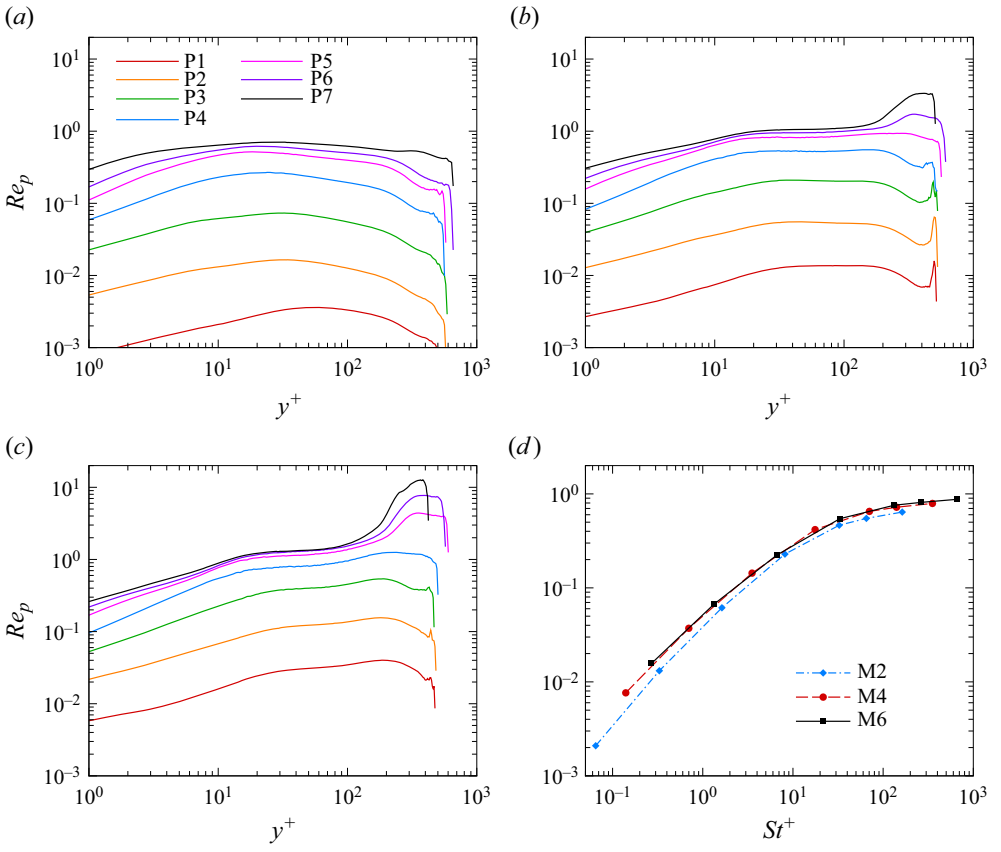

Figure 18. Mean particle Reynolds number $\overline{Re_p}$ in (*a*) case M2, (*b*) case M4, (*c*) case M6; and (*d*) at $y^+ = 10$ for the three flow cases.

and Mach numbers, especially the latter due to the manifestation of the Mach number dependence.

For the purpose of exploring the cause disparity in $\bar{a}_1\tau_p$ and $\bar{a}_2\tau_p$ in high Stokes number particles, we further discuss the two factors in the expression of f_D, namely the particle Reynolds numbers Re_p and the particle Mach numbers M_p. In figure 18(*a–c*), we present the wall-normal distribution of the mean particle Reynolds number $\overline{Re_p}$ in the cases at different free stream Mach numbers. As St^+ increases, $\overline{Re_p}$ increases monotonically across the boundary layer. Since the diameters are same for different particle populations, the increment of $\overline{Re_p}$ should be attributed primarily to the differences in the slip velocity, local fluid density and viscosity. In most of the region, $\overline{Re_p}$ remains low-valued at no higher than 5.0, a criterion below which the flow surrounding the particle can be regarded as creeping flow without shedding vortices. Even near the edge of the boundary layer, the highest particle Reynolds number is merely 10. We have also inspected the probability density function (PDF) of Re_p in both the near-wall and outer regions, and found that the probability of Re_p exceeding 20 is less than 1 %. The comparatively high values of $\overline{Re_p}$ near the edge of the boundary layer in case M6, as shown in figure 18(*c*), could be caused by the very rare occurrence of the particles reaching that location, thereby highlighting the comparatively high Reynolds number ones. Figure 18(*d*) further demonstrates that $\overline{Re_p}$ at

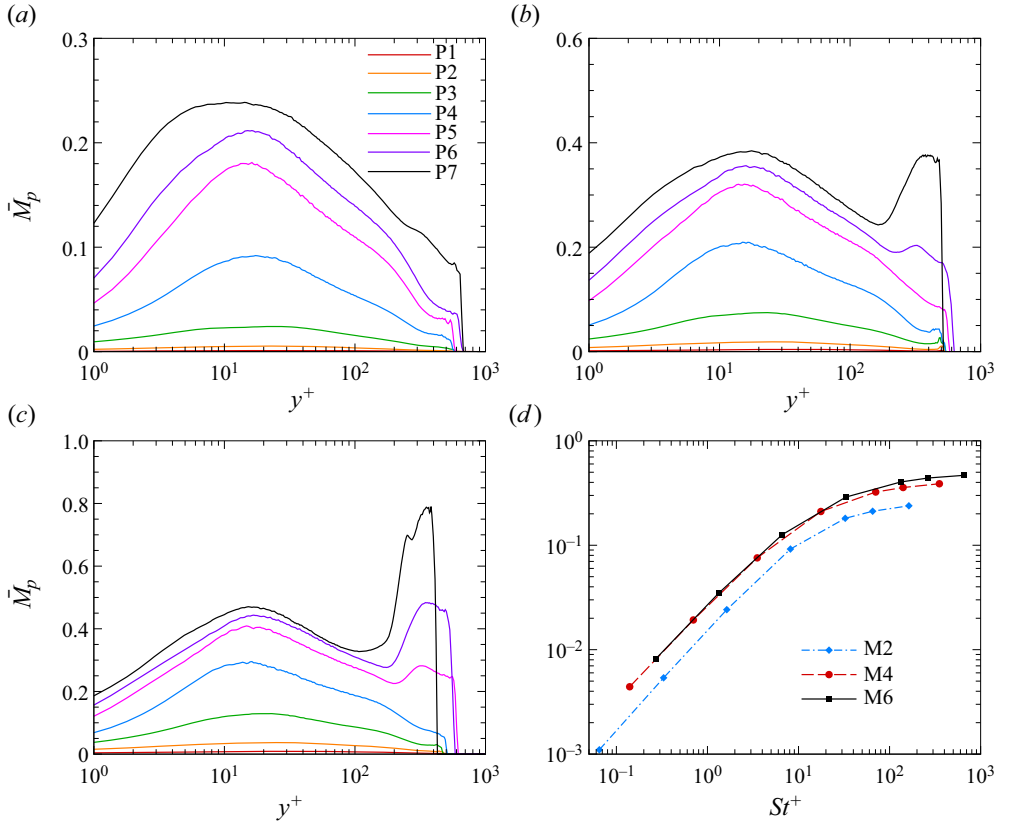

Figure 19. Mean particle Mach number $\bar{M}_p$ in (*a*) case M2, (*b*) case M4, (*c*) case M6; and (*d*) the near-wall maximum.

$y^+ = 10$ is also weakly dependent on the Mach number, showing a slight augmentation with M_∞. Under such circumstances, the refinement of the drag force regarding the high Reynolds number effects is expected, at least statistically.

Figure 19 displays the wall-normal distribution of the mean particle Mach number $\bar{M}_p$. Consistent with the trend of variation of the flow quantities discussed above, $\bar{M}_p$ increases with St^+ due to their comparatively high mean and fluctuating slip velocities, and also with the free stream Mach number. At the free stream Mach number $M_\infty = 2$, there manifests only one peak in the profiles of $\bar{M}_p$ for each particle population in the buffer region where the turbulent fluctuations are the most intense, whereas at $M_\infty = 4$ and 6, there gradually emerge second peaks in the outer region, the values of which even exceed the near-wall peak values for large-inertia particles. Nevertheless, in the presently considered cases, there is no such a region where the particles are slipping at supersonic speed in the average sense. The near-wall peaks of $\bar{M}_p$ (figure 19*d*) increase monotonically with the Stokes number St^+ but incline to converge to the near-wall maximum of the turbulent Mach number, which is defined by the turbulent kinetic energy and the local mean acoustic velocity.

We further report the PDF of the particle Mach number M_p in the near-wall region below $y^+ = 10$ (figures 20*a*,*c*,*e*) and in the outer region within $y = (0.6\text{–}2.0)\delta$ (figures 20*b*,*d*,*f*). It is interesting to note that the probability of the high Stokes number particle slipping at

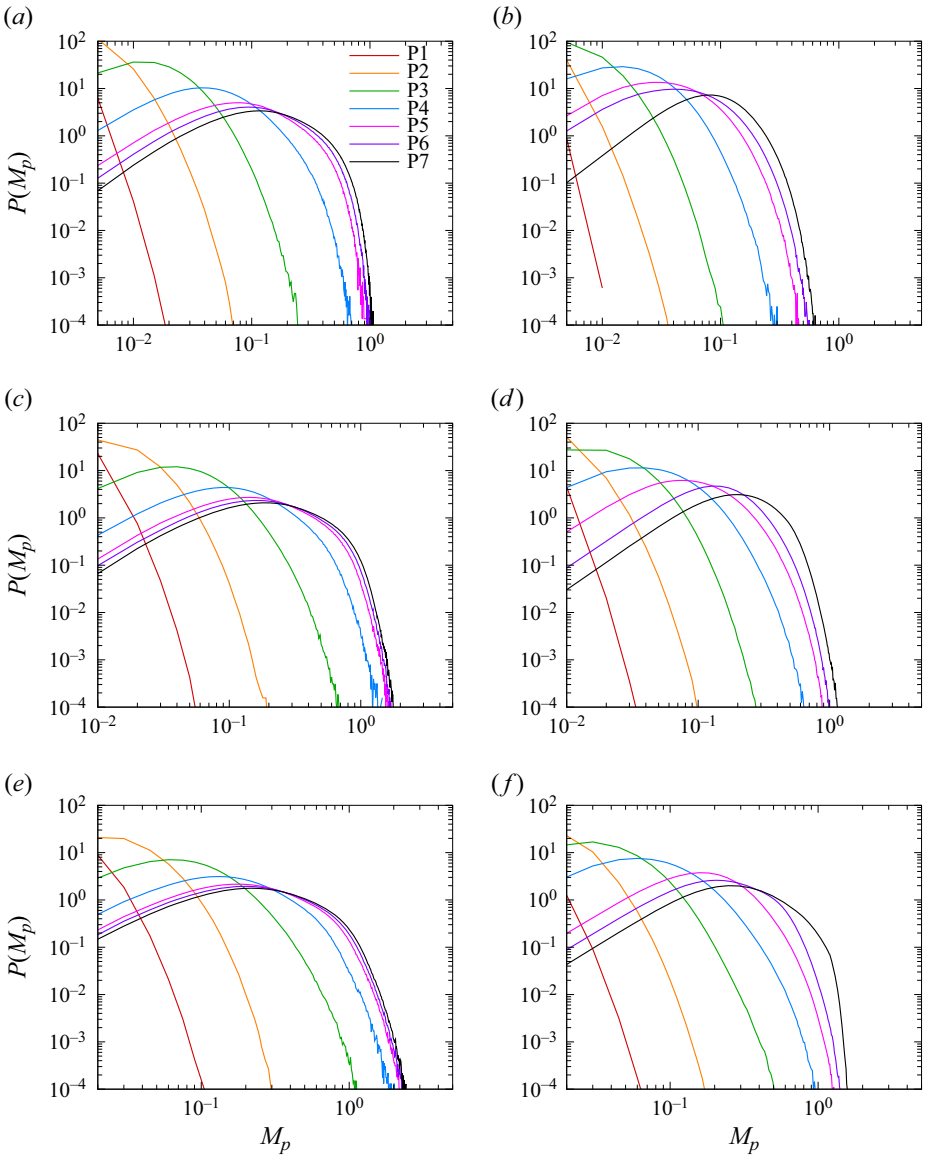

Figure 20. The PDF of particle Mach number M_p (a,c,e) below $y^+ = 10$ and (b,d,f) in the outer region within $y = (0.6\text{–}2.0)\delta$, for ($a$,$b$) case M2, ($c$,$d$) case M4, and ($e$,$f$) case M6.

supersonic speed in cases M4 and M6 is higher in the near-wall region than in the outer region, as indicated by both their higher values and wider ranges of the PDF distributions. Such higher particle Mach numbers induce higher drag force, not only in their mean values but also in their fluctuations, the integration of which in time will lead to further disparities in the statistics of the particle velocity. This serves as a possible explanation for the different behaviours of the particle velocity fluctuations with large St^+ at various Mach numbers (recall figure 13).

To further explore the Reynolds number and Mach number effects on the drag force, in figure 21 we present the joint PDFs between Re_p and M_p below $y^+ = 10$, pre-multiplied

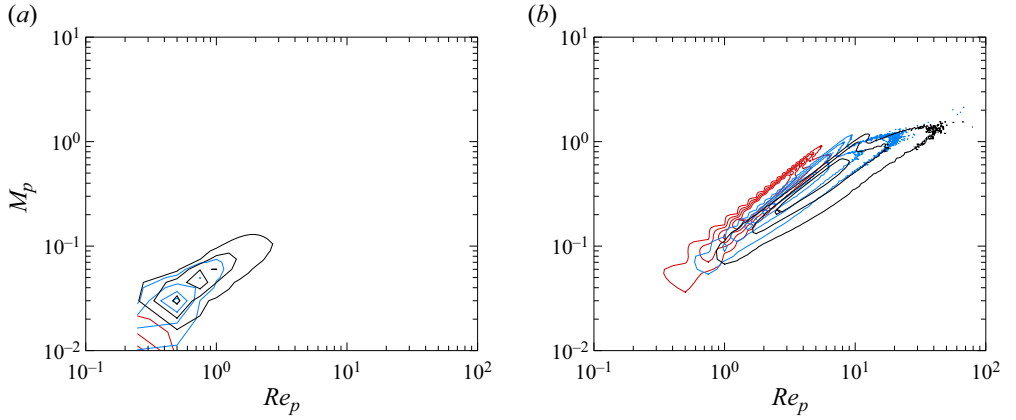

Figure 21. Pre-multiplied joint PDFs between Re_p and M_p ($f_D\, Re_p\, M_p\, P(Re_p, M_p)$) of particle populations (*a*) P2, (*b*) P7 for case M2, P6 for case M4, and P5 for case M6. Red lines indicate M2; blue lines indicate M4; black lines indicate M6. Contour levels are (0.1, 0.5, 1.0, 1.5).

by f_D, M_p and Re_p. The integration of the PDF under double logarithmic coordinates gives the mean values of f_D, corresponding to the modification of the drag forces by high Re_p and M_p. For particle population P2 (figure 21*a*), the pre-multiplied joint PDFs are mainly concentrated in the low Re_p and M_p region, with no significant difference in their distributions at different M_∞. For higher Stokes number particles, however, such disparity can be visualized clearly, as demonstrated in figure 21(*b*), where particle populations P7 in case M2, P6 in case M4, and P5 in case M6 are presented due to their approximately the same St^+ (≈ 150). At higher M_∞, the high values of the pre-multiplied joint PDF extend to the regions of both higher Re_p and higher M_p, suggesting that the drag forces acting on the particles in high Mach number cases are stronger. This is consistent with the higher acceleration shown in figure 17, but lower velocity fluctuations presented in figure 13, supporting our inferences in the discussion above.

5. Conclusions

In the present study, we perform direct numerical simulations of compressible turbulent boundary layer flow at Mach numbers 2, 4 and 6 that transport the dilute phase of spherical particles utilizing the point-particle Eulerian–Lagrangian framework. We consider seven particle populations, covering a wide range of Stokes numbers, and examine the instantaneous and statistical distributions, and the mean and fluctuating particle velocities, with the focus on their consistency and discrepancies at different Mach numbers.

In the instantaneous flow fields, it is found that the distributions of the low Stokes number particles resemble those of the density, restricted within the turbulent boundary layers, which can be explained by the identical form of the continuity equation and the approximation of the transport equation of the particle concentration field. The high Stokes number particles, on the other hand, are capable of escaping the 'restriction' of the turbulent–non-turbulent interface and reaching the free stream due to their large inertia. The particles with moderate Stokes numbers tend to accumulate near the wall, known as the turbophoresis, and manifest clustering beneath the low-speed region, consistent with the findings in incompressible canonical wall-bounded turbulence.

Quantitatively, however, the degrees of both near-wall accumulation and small-scale clustering, evaluated by the Shannon entropy and the power-law scaling of the radial density function at $r \to 0$, respectively, are slightly reduced by the higher free stream Mach number, whereas that of clustering remains unaffected.

The distribution of the particles can be reflected by the mean fluid velocity seen by particles in that the particle streamwise velocities are lower than the mean fluid velocity with moderate Stokes numbers, while the wall-normal velocities are higher. The profiles of the streamwise mean particle velocity are flatter with increasing Stokes number considering their slow response to the fluid motion when travelling vertically, whereas the wall-normal mean velocities are approximately independent of the particle inertia, merely showing the spatial development of the boundary layer. As for the particle fluctuating velocity, the streamwise component shows non-monotonic variation against the Stokes number and relevance to the Mach number, while the wall-normal component decreases monotonically and depends weakly on the Mach number. By inspecting the statistics of the particle acceleration and the factors by which it is influenced, we prove that the increasing particle Reynolds and Mach numbers lead to the variation of the streamwise particle velocity fluctuations for large Stokes number particles.

The present work systematically studies the transport of particles with various Stokes numbers in the compressible turbulent boundary layers, but only one-way coupling is concerned. Future work will be dedicated to the investigation of the two-way coupling effects that incorporate the particle feedback to the phase of fluid turbulence.

Funding. This work is supported by the National Natural Science Foundation of China (grant nos 12202469, 92052301, 92252104, 12388101).

Declaration of interests. The authors report no conflict of interest.

Author ORCIDs.
Ming Yu https://orcid.org/0000-0001-7772-833X;
Lihao Zhao https://orcid.org/0000-0002-3642-3051;
Xianxu Yuan https://orcid.org/0000-0002-7668-0116;
Chunxiao Xu https://orcid.org/0000-0001-5292-8052.

Appendix A. Validation of the numerical solver

We perform DNS of the turbulent channel flows at the friction Reynolds number $Re_\tau = \rho_w u_\tau h/\mu_w = 180$ and bulk Mach number $M_b = u_b/\sqrt{\gamma R T_w} = 0.3$ for the validation of the numerical solver utilized in the present study. The simulation is performed in the computational domain with the streamwise and spanwise sizes of $2\pi h$ and πh, respectively, with h the half-channel height. Four types of particles, with Stokes numbers $St^+ = 1$, 10, 50 and 200, are injected uniformly into the channel after the turbulence is fully developed. The statistics are collected within the time span $7000\delta_v/u_\tau$ after the simulation has been run for $7000\delta_v/u_\tau$. The results are compared with those obtained by the incompressible turbulent channel flow solvers developed by Jie *et al.* (2022), Cui & Zhao (2022) and Cui *et al.* (2021) (the DNS solvers are obtained via private communication) under the same parameter settings. As reported in figure 22, the streamwise mean particle velocity $\bar{v}_1$, mean particle concentration $\bar{c}(y)$, and RMS of the streamwise and wall-normal particle velocities obtained by the two distinct solvers agree well with each other, consolidating the accuracy of the two-phase DNS solver utilized in the present study.

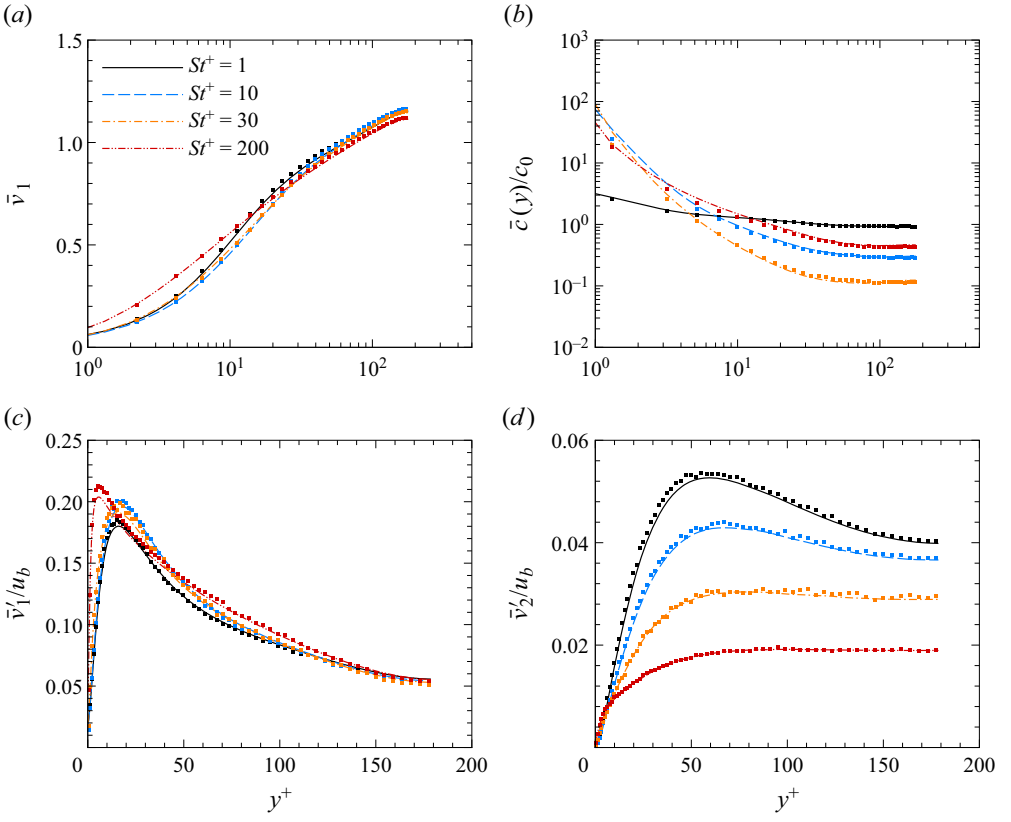

Figure 22. Particle statistics in a turbulent channel flow: (*a*) $\bar{v}_1$, (*b*) $\bar{c}(y)/c_0$, (*c*) $\bar{v}_1'$, (*d*) $\bar{v}_2'$. Here, u_b is the bulk velocity of the channel. Lines indicate the present study; symbols indicate reference data of incompressible flows (Jie *et al.* 2022).

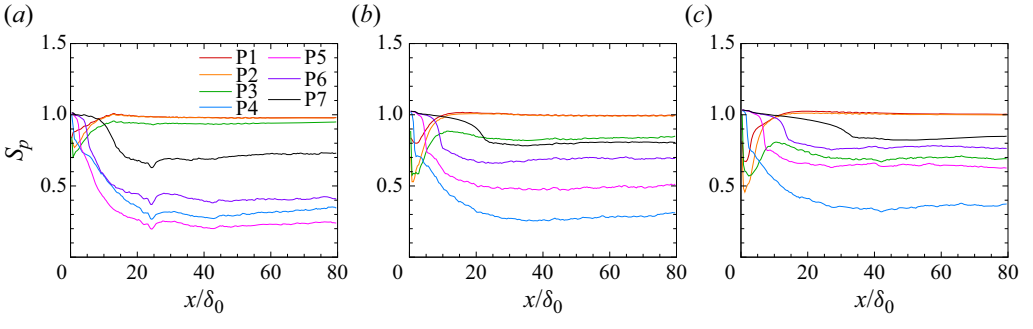

Figure 23. Streamwise variation of the Shannon entropy S_p in cases (*a*) M2, (*b*) M4 and (*c*) M6.

Appendix B. Streamwise variation of the Shannon entropy

For the validation of the streamwise statistical invariance within $(60–70)\delta_0$, in figure 23 we present the variation of the Shannon entropy S_p defined in § 3.2, which is usually adopted for the purpose of verifying the convergence and depicting the degree of near-wall accumulation (Picano *et al.* 2009; Bernardini 2014). For all the cases considered, the Shannon entropy S_p for each particle population remains almost constant, suggesting

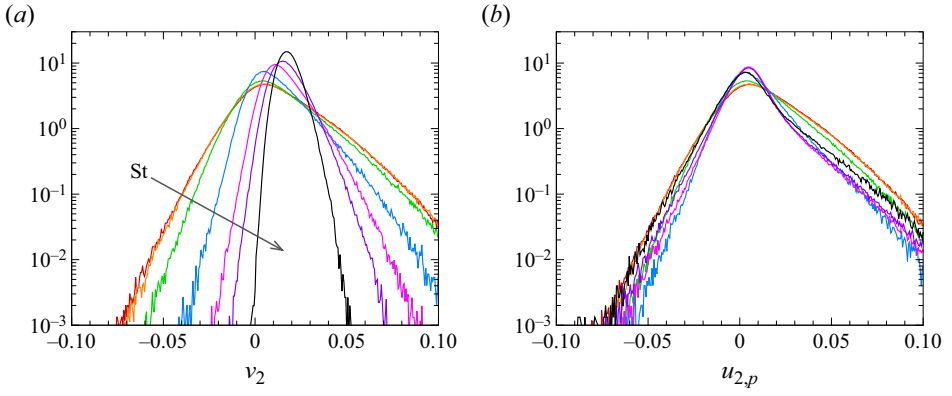

Figure 24. The PDFs of (*a*) v_2 and (*b*) $u_{2,p}$ above $y = 0.6\delta$ in case M4. For line legend, refer to figure 20.

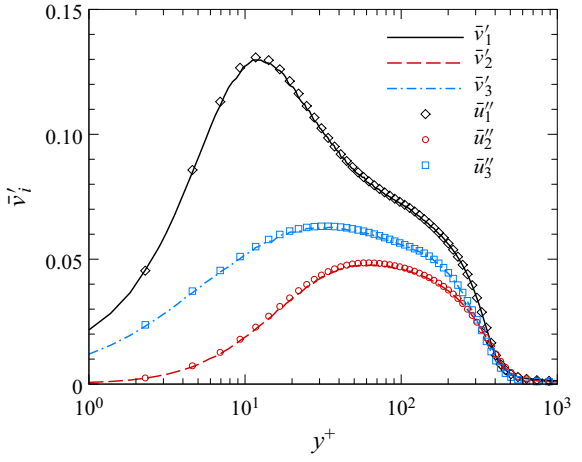

Figure 25. RMS of particle (P1) and fluid velocity fluctuations in case M2, with the particles released randomly at the flow inlet across the whole wall-normal computational domain.

that the particle distributions are statistically steady and quasi-homogeneous, in particular within the domain of interest (60–70)δ_0 where the statistics are obtained.

Appendix C. The PDF of wall-normal fluid velocity seen by particles

In figure 24, we present the PDFs of the wall-normal particle velocity v_2 and the fluid velocity seen by particles $u_{2,p}$ above $y = 0.6\delta$ in case M4. Obviously, the PDF values are higher in the positive regions than those in the negative regions, supporting our statement that the particles prefer to accumulate by the strong ejections.

Appendix D. Particle velocity fluctuations with a different flow inlet condition

We have inferred in § 4.1 that the discrepancies in the RMS of the velocity fluctuations between the particle and fluid should be ascribed to the distribution of the particles within the boundary layer thickness. In this appendix, we attempt to verify this inference by performing an extra simulation with the same computational settings as in case M2, except that the particles are released randomly at the flow inlet across the whole wall-normal

computational domain instead of merely within δ_0. The obtained RMS of the particle (population P1) and fluid velocity fluctuations are shown in figure 25. The profiles are well collapsed, especially near the edge of the boundary layer, validating the correctness of the inference in § 4.1.

References

Armenio, V. & Fiorotto, V. 2001 The importance of the forces acting on particles in turbulent flows. *Phys. Fluids* **13** (8), 2437–2440.

Balachandar, S. 2009 A scaling analysis for point-particle approaches to turbulent multiphase flows. *Intl J. Multiphase Flow* **35** (9), 801–810.

Balachandar, S. & Eaton, J.K. 2010 Turbulent dispersed multiphase flow. *Annu. Rev. Fluid Mech.* **42**, 111–133.

Balkovsky, E., Falkovich, G. & Fouxon, A. 2001 Intermittent distribution of inertial particles in turbulent flows. *Phys. Rev. Lett.* **86** (13), 2790.

Baltussen, M.W., Buist, K.A., Peters, E. & Kuipers, J. 2018 Multiscale modelling of dense gas–particle flows. In *Bridging Scales in Modelling and Simulation of Non-Reacting and Reacting Flows. Part II* (ed. A. Parente & J. De Wilde), *Advances in Chemical Engineering*, vol. 53, pp. 1–52. Academic Press.

Bec, J., Biferale, L., Cencini, M., Lanotte, A., Musacchio, S. & Toschi, F. 2007 Heavy particle concentration in turbulence at dissipative and inertial scales. *Phys. Rev. Lett.* **98** (8), 084502.

Berk, T. & Coletti, F. 2020 Transport of inertial particles in high-Reynolds-number turbulent boundary layers. *J. Fluid Mech.* **903**, A18.

Bernardini, M. 2014 Reynolds number scaling of inertial particle statistics in turbulent channel flows. *J. Fluid Mech.* **758**, R1.

Bernardini, M., Modesti, D., Salvadore, F. & Pirozzoli, S. 2021 STREAmS: a high-fidelity accelerated solver for direct numerical simulation of compressible turbulent flows. *Comput. Phys. Commun.* **263**, 107906.

Bernardini, M. & Pirozzoli, S. 2011 Wall pressure fluctuations beneath supersonic turbulent boundary layers. *Phys. Fluids* **23** (8), 085102.

Bernardini, M., Pirozzoli, S. & Orlandi, P. 2013 The effect of large-scale turbulent structures on particle dispersion in wall-bounded flows. *Intl J. Multiphase. Flow* **51**, 55–64.

Bragg, A.D. & Collins, L.R. 2014 New insights from comparing statistical theories for inertial particles in turbulence: I. Spatial distribution of particles. *New J. Phys.* **16** (5), 055013.

Brandt, L. & Coletti, F. 2022 Particle-laden turbulence: progress and perspectives. *Annu. Rev. Fluid Mech.* **54**, 159–189.

Buchta, D.A., Shallcross, G. & Capecelatro, J. 2019 Sound and turbulence modulation by particles in high-speed shear flows. *J. Fluid Mech.* **875**, 254–285.

Cao, Y.H., Wu, Z.L. & Xu, Z.Y. 2014 Effects of rainfall on aircraft aerodynamics. *Prog. Aerosp. Sci.* **71**, 85–127.

Capecelatro, J. & Wagner, J.L. 2024 Gas–particle dynamics in high-speed flows. *Annu. Rev. Fluid Mech.* **56**, 379–403.

Casciola, C.M., Gualtieri, P., Jacob, B. & Piva, R. 2007 The residual anisotropy at small scales in high shear turbulence. *Phys. Fluids* **19** (10), 101704.

Cheng, X.L., Zeng, Q.C. & Hu, F. 2012 Stochastic modeling the effect of wind gust on dust entrainment during sand storm. *Chin. Sci. Bull.* **57**, 3595–3602.

Clift, R. & Gauvin, W.H. 1971 Motion of entrained particles in gas streams. *Can. J. Chem. Engng* **49** (4), 439–448.

Cogo, M., Salvadore, F., Picano, F. & Bernardini, M. 2022 Direct numerical simulation of supersonic and hypersonic turbulent boundary layers at moderate–high Reynolds numbers and isothermal wall condition. *J. Fluid Mech.* **945**, A30.

Crowe, C.T., Troutt, T.R. & Chung, J.N. 1996 Numerical models for two-phase turbulent flows. *Annu. Rev. Fluid Mech.* **28** (1), 11–43.

Cui, Z.W., Huang, W.X., Xu, C.X., Andersson, H.I. & Zhao, L.H. 2021 Alignment of slender fibers and thin disks induced by coherent structures of wall turbulence. *Intl J. Multiphase Flow* **145**, 103837.

Cui, Z.W. & Zhao, L.H. 2022 Shape-dependent regions for inertialess spheroids in turbulent channel flow. *Phys. Fluids* **34** (12), 123316.

DAI, Q., JIN, T., LUO, K. & FAN, J.R. 2018 Direct numerical simulation of particle dispersion in a three-dimensional spatially developing compressible mixing layer. *Phys. Fluids* **30** (11), 113301.

DAI, Q., JIN, T., LUO, K., XIAO, W. & FAN, J.R. 2019 Direct numerical simulation of a three-dimensional spatially evolving compressible mixing layer laden with particles. II. Turbulence anisotropy and growth rate. *Phys. Fluids* **31** (8), 083303.

DAI, Q., LUO, K., JIN, T. & FAN, J.R. 2017 Direct numerical simulation of turbulence modulation by particles in compressible isotropic turbulence. *J. Fluid Mech.* **832**, 438–482.

DUCROS, F., FERRAND, V., NICOUD, F., WEBER, C., DARRACQ, D., GACHERIEU, C. & POINSOT, T. 1999 Large-eddy simulation of the shock/turbulence interaction. *J. Comput. Phys.* **152** (2), 517–549.

EATON, J.K. 2009 Two-way coupled turbulence simulations of gas–particle flows using point-particle tracking. *Intl J. Multiphase Flow* **35** (9), 792–800.

EATON, J.K. & FESSLER, J.R. 1994 Preferential concentration of particles by turbulence. *Intl J. Multiphase Flow* **20**, 169–209.

ELGHOBASHI, S. 1994 On predicting particle-laden turbulent flows. *Appl. Sci. Res.* **52**, 309–329.

FENG, Y., LUO, S., SONG, J. & XU, D. 2023*b* Numerical investigation on flow and mixing characteristics of powder fuel under strong shear and shock wave interaction. *Energy* **263**, 126061.

FENG, Y.B., LUO, S.B., SONG, J.W., XIA, K.X. & XU, D.Q. 2023*a* Numerical investigation on the combustion characteristics of aluminum powder fuel in a supersonic cavity-based combustor. *Appl. Therm. Engng* **221**, 119842.

FERRY, J. & BALACHANDAR, S. 2001 A fast Eulerian method for disperse two-phase flow. *Intl J. Multiphase Flow* **27** (7), 1199–1226.

FERRY, J. & BALACHANDAR, S. 2002 Equilibrium expansion for the Eulerian velocity of small particles. *Powder Technol.* **125** (2–3), 131–139.

FESSLER, J.R., KULICK, J.D. & EATON, J.K. 1994 Preferential concentration of heavy particles in a turbulent channel flow. *Phys. Fluids* **6** (11), 3742–3749.

FONG, K.O., AMILI, O. & COLETTI, F. 2019 Velocity and spatial distribution of inertial particles in a turbulent channel flow. *J. Fluid Mech.* **872**, 367–406.

GAO, W., SAMTANEY, R. & RICHTER, D.H. 2023 Direct numerical simulation of particle-laden flow in an open channel at $Re_\tau = 5186$. *J. Fluid Mech.* **957**, A3.

GOTO, S. & VASSILICOS, J.C. 2008 Sweep-stick mechanism of heavy particle clustering in fluid turbulence. *Phys. Rev. Lett.* **100** (5), 054503.

GUALTIERI, P., PICANO, F. & CASCIOLA, C.M. 2009 Anisotropic clustering of inertial particles in homogeneous shear flow. *J. Fluid Mech.* **629**, 25–39.

HWANG, Y. 2013 Near-wall turbulent fluctuations in the absence of wide outer motions. *J. Fluid Mech.* **723**, 264–288.

JIE, Y., ANDERSSON, H.I. & ZHAO, L.H. 2021 Effects of the quiescent core in turbulent channel flow on transport and clustering of inertial particles. *Intl J. Multiphase Flow* **140**, 103627.

JIE, Y.C., CUI, Z.W., XU, C.X. & ZHAO, L.H. 2022 On the existence and formation of multi-scale particle streaks in turbulent channel flows. *J. Fluid Mech.* **935**, A18.

JIMÉNEZ, J. 2013 Near-wall turbulence. *Phys. Fluids* **25** (10), 101302.

JIMÉNEZ, J. 2018 Coherent structures in wall-bounded turbulence. *J. Fluid Mech.* **842**, P1.

KENNEDY, C.A. & GRUBER, A. 2008 Reduced aliasing formulations of the convective terms within the Navier–Stokes equations for a compressible fluid. *J. Comput. Phys.* **227** (3), 1676–1700.

KLEIN, M., SADIKI, A. & JANICKA, J. 2003 A digital filter based generation of inflow data for spatially developing direct numerical or large eddy simulations. *J. Comput. Phys.* **186** (2), 652–665.

KUERTEN, M.J.G. 2016 Point-particle DNS and LES of particle-laden turbulent flow – a state-of-the-art review. *Flow Turbul. Combust.* **97**, 689–713.

KULICK, J.D., FESSLER, J.R. & EATON, J.K. 1994 Particle response and turbulence modification in fully developed channel flow. *J. Fluid Mech.* **277**, 109–134.

KWON, Y.S., PHILIP, J., DE SILVA, C.M., HUTCHINS, N. & MONTY, J.P. 2014 The quiescent core of turbulent channel flow. *J. Fluid Mech.* **751**, 228–254.

LI, T., CUI, Z.W., YUAN, X.X., ZHANG, Y., ZHOU, Q. & ZHAO, L.H. 2023 Particle dynamics in compressible turbulent vertical channel flows. *Phys. Fluids* **35** (8), 083332.

LI, Z.Z., WEI, J.J. & YU, B. 2016 Direct numerical study on effect of interparticle collision in particle-laden turbulence. *AIAA J.* **54** (10), 3212–3222.

LIU, H.Y. & ZHENG, X.J. 2021 Large-scale structures of wall-bounded turbulence in single- and two-phase flows: advancing understanding of the atmospheric surface layer during sandstorms. *Flow* **1**, E5.

LOTH, E., TYLER DASPIT, J., JEONG, M., NAGATA, T. & NONOMURA, T. 2021 Supersonic and hypersonic drag coefficients for a sphere. *AIAA J.* **59** (8), 3261–3274.

MARCHIOLI, C. & SOLDATI, A. 2002 Mechanisms for particle transfer and segregation in a turbulent boundary layer. *J. Fluid Mech.* **468**, 283–315.

MARCHIOLI, C., SOLDATI, A., KUERTEN, J.G.M., ARCEN, B., TANIERE, A., GOLDENSOPH, G., SQUIRES, K.D., CARGNELUTTI, M.F. & PORTELA, L.M. 2008 Statistics of particle dispersion in direct numerical simulations of wall-bounded turbulence: results of an international collaborative benchmark test. *Intl J. Multiphase Flow* **34** (9), 879–893.

MAXEY, M.R. & RILEY, J.J. 1983 Equation of motion for a small rigid sphere in a nonuniform flow. *Phys. Fluids* **26** (4), 883–889.

MILICI, B. & DE MARCHIS, M. 2016 Statistics of inertial particle deviation from fluid particle trajectories in horizontal rough wall turbulent channel flow. *Intl J. Heat Fluid Flow* **60**, 1–11.

MONCHAUX, R., BOURGOIN, M. & CARTELLIER, A. 2010 Preferential concentration of heavy particles: a Voronoï analysis. *Phys. Fluids* **22** (10), 103304.

MONCHAUX, R., BOURGOIN, M. & CARTELLIER, A. 2012 Analyzing preferential concentration and clustering of inertial particles in turbulence. *Intl J. Multiphase Flow* **40**, 1–18.

MORTIMER, L.F. & FAIRWEATHER, M. 2020 Density ratio effects on the topology of coherent turbulent structures in two-way coupled particle-laden channel flows. *Phys. Fluids* **32** (10), 103302.

MORTIMER, L.F., NJOBUENWU, D.O. & FAIRWEATHER, M. 2019 Near-wall dynamics of inertial particles in dilute turbulent channel flows. *Phys. Fluids* **31** (6), 063302.

MOTOORI, Y., WONG, C. & GOTO, S. 2022 Role of the hierarchy of coherent structures in the transport of heavy small particles in turbulent channel flow. *J. Fluid Mech.* **942**, A3.

MUSKER, A. 1979 Explicit expression for the smooth wall velocity distribution in a turbulent boundary layer. *AIAA J.* **17** (6), 655–657.

NARAYANAN, C., LAKEHAL, D., BOTTO, L. & SOLDATI, A. 2003 Mechanisms of particle deposition in a fully developed turbulent open channel flow. *Phys. Fluids* **15** (3), 763–775.

PICANO, F., SARDINA, G. & CASCIOLA, C.M. 2009 Spatial development of particle-laden turbulent pipe flow. *Phys. Fluids* **21** (9), 093305.

PICCIOTTO, M., MARCHIOLI, C., REEKS, M.W. & SOLDATI, A. 2005*a* Statistics of velocity and preferential accumulation of micro-particles in boundary layer turbulence. *Nucl. Engng Des.* **235** (10–12), 1239–1249.

PICCIOTTO, M., MARCHIOLI, C. & SOLDATI, A. 2005*b* Characterization of near-wall accumulation regions for inertial particles in turbulent boundary layers. *Phys. Fluids* **17** (9), 098101.

PIROZZOLI, S. 2010 Generalized conservative approximations of split convective derivative operators. *J. Comput. Phys.* **229** (19), 7180–7190.

PIROZZOLI, S. 2011 Numerical methods for high-speed flows. *Annu. Rev. Fluid Mech.* **43**, 163–194.

PUMIR, A. & WILKINSON, M. 2016 Collisional aggregation due to turbulence. *Annu. Rev. Condens. Matt. Phys.* **7**, 141–170.

RASHIDI, M., HETSRONI, G. & BANERJEE, S. 1990 Particle–turbulence interaction in a boundary layer. *Intl J. Multiphase Flow* **16** (6), 935–949.

ROUSON, D. & EATON, J.K. 2001 On the preferential concentration of solid particles in turbulent channel flow. *J. Fluid Mech.* **428**, 149–169.

RUDINGER, G. 2012 *Fundamentals of Gas–Particle Flow*, vol. 2. Elsevier.

SALAZAR, J., DE JONG, J., CAO, L., WOODWARD, S.H., MENG, H. & COLLINS, L. 2008 Experimental and numerical investigation of inertial particle clustering in isotropic turbulence. *J. Fluid Mech.* **600**, 245–256.

SARDINA, G., SCHLATTER, P., BRANDT, L., PICANO, F. & CASCIOLA, C.M. 2012 Wall accumulation and spatial localization in particle-laden wall flows. *J. Fluid Mech.* **699**, 50–78.

SAW, E.W., SHAW, R.A., AYYALASOMAYAJULA, S., CHUANG, P.Y. & GYLFASON, A. 2008 Inertial clustering of particles in high-Reynolds-number turbulence. *Phys. Rev. Lett.* **100** (21), 214501.

SHU, C.W. & OSHER, S. 1988 Efficient implementation of essentially non-oscillatory shock-capturing schemes. *J. Comput. Phys.* **77** (2), 439–471.

SOLDATI, A. 2005 Particles turbulence interactions in boundary layers. *Z. Angew. Math. Mech.* **85** (10), 683–699.

SOLDATI, A. & MARCHIOLI, C. 2009 Physics and modelling of turbulent particle deposition and entrainment: review of a systematic study. *Intl J. Multiphase Flow* **35** (9), 827–839.

TARDU, S. 1995 Characteristics of single and clusters of bursting events in the inner layer. *Exp. Fluids* **20** (2), 112–124.

VINKOVIC, I., DOPPLER, D., LELOUVETEL, J. & BUFFAT, M. 2011 Direct numerical simulation of particle interaction with ejections in turbulent channel flows. *Intl J. Multiphase Flow* **37** (2), 187–197.

WANG, L.P. & MAXEY, M.R. 1993 Settling velocity and concentration distribution of heavy particles in homogeneous isotropic turbulence. *J. Fluid Mech.* **256**, 27–68.

WANG, X., WAN, M. & BIFERALE, L. 2022 Acceleration statistics of tracer and light particles in compressible homogeneous isotropic turbulence. *J. Fluid Mech.* **935**, A36.

WANG, Y.S., HUANG, W.X. & XU, C.X. 2015 On hairpin vortex generation from near-wall streamwise vortices. *Acta Mechanica Sin.* **31**, 139–152.

WRAY, A. 1990 Minimal storage time advancement schemes for spectral methods. *Report no.* MS 202. NASA Ames Research Center, California.

XIAO, W., JIN, T., LUO, K., DAI, Q. & FAN, J.R. 2020 Eulerian–Lagrangian direct numerical simulation of preferential accumulation of inertial particles in a compressible turbulent boundary layer. *J. Fluid Mech.* **903**, A19.

YANG, Y., WANG, J., SHI, Y., XIAO, Z., HE, X.T. & CHEN, S.Y. 2014 Interactions between inertial particles and shocklets in compressible turbulent flow. *Phys. Fluids* **26** (9), 091702.

YU, M. & XU, C.X. 2021 Compressibility effects on hypersonic turbulent channel flow with cold walls. *Phys. Fluids* **33** (7), 075106.

YU, M., XU, C.X. & PIROZZOLI, S. 2019 Genuine compressibility effects in wall-bounded turbulence. *Phys. Rev. Fluids* **4** (12), 123402.

YU, Z.S., LIN, Z.W., SHAO, X.M. & WANG, L.P. 2017 Effects of particle–fluid density ratio on the interactions between the turbulent channel flow and finite-size particles. *Phys. Rev.* E **96** (3), 033102.

ZHANG, Q.Q., LIU, H., MA, Z.Q. & XIAO, Z.L. 2016 Preferential concentration of heavy particles in compressible isotropic turbulence. *Phys. Fluids* **28** (5), 055104.

ZHANG, Y., BI, W., HUSSAIN, F. & SHE, Z. 2014 A generalized Reynolds analogy for compressible wall-bounded turbulent flows. *J. Fluid Mech.* **739**, 392–420.

ZHAO, L.H., MARCHIOLI, C. & ANDERSSON, H.I. 2012 Stokes number effects on particle slip velocity in wall-bounded turbulence and implications for dispersion models. *Phys. Fluids* **24** (2), 021705.